Single-Frame MIMO Radar Velocity Vector Estimation via Multi-Bounce Scattering

Nishant Mehrotra, Divyanshu Pandey, Upamanyu Madhow, *Fellow, IEEE*, Yasamin Mostofi, *Fellow, IEEE*, and Ashutosh Sabharwal, *Fellow, IEEE*

***Abstract*—Radars are widely adopted for autonomous navigation and vehicular networking due to their robustness to weather conditions as compared to visible light cameras and lidars. However, radars currently struggle with differentiating static vs tangentially moving objects within a *single radar frame* since both yield the same Doppler along line-of-sight paths to the radar. Prior solutions deploy multiple radar or visible light camera modules to form a multi-"look" synthetic aperture for estimating the single-frame velocity vectors, to estimate tangential and radial velocity components of moving objects leading to higher system costs. In this paper, we propose to exploit multi-bounce scattering from secondary static objects in the environment, e.g., building pillars, walls, etc., to form an effective multi-"look" synthetic aperture for single-frame velocity vector estimation with a *single* multiple-input, multiple-output (MIMO) radar, thus reducing the overall system cost and removing the need for multi-module synchronization. We present a comprehensive theoretical and experiment evaluation of our scheme, demonstrating a $4.5\times$ reduction in the error for estimating moving objects' velocity vectors over comparable single-radar baselines.**

***Index Terms*—MIMO radar, multipath, radar imaging, synthetic aperture radar, velocity measurement.**

I. Introduction

RADARS are an indispensable sensing modality for autonomous navigation and vehicular networking, with multiple advantages over visible light cameras and lidars [2], [3], [4]: (i) lower cost, (ii) smaller sensor size, and (iii) robustness to lighting and weather conditions (fog, smoke, etc.). Traditional radar signal processing models line-of-sight (LOS) scattering from objects that are directly illuminated by the radar and scatter the illumination back. LOS radar processing enables estimating the range and radial velocity of objects, as well as their azimuth and elevation angles [2], [4], [5] when the radar is equipped with multiple transmit and receive antennas, often labeled as multiple-input, multiple-output (MIMO) radar.[1] There are two main advantages of LOS radar processing: (i) high signal-to-noise ratios (SNRs) due to limited attenuation besides two-way propagation, radar → object → radar, and reflection loss at the object, and (ii) low-complexity implementation via fast Fourier transforms (FFTs).

Despite the above advantages, LOS radar processing cannot estimate the *tangential velocities* of moving objects (except in certain limiting cases surveyed in more detail in Section I-B). No tangential velocity estimation limits radar performance in scenarios where objects move tangentially to the radar [6], e.g., cross-moving cars and pedestrians at a traffic intersection. This work tackles the problem of estimating both the radial and tangential velocities, i.e., the *velocity vectors*, of moving objects using non-line-of-sight (NLOS) radar signal processing. In this paper, we use *multi-bounce* as a general term to indicate signal components scattering more than once from objects in the environment, e.g., *single-bounce* to denote LOS paths between the radar and moving objects (since the radar signals bounce once at the objects before being received back at the radar), and *double-bounce* and *triple-bounce* to denote paths that scatter twice and thrice.

A. Overview of Main Contributions

We propose to exploit multi-bounce signals and thereby enable a *single* MIMO radar to estimate the *single-frame*[2] velocity vectors of moving objects in the environment. The key idea is illustrated for a MIMO radar tracking a person walking near a building pillar in Fig. 1. The radial velocity of the person falls along the radar's LOS to the person: radar → object → radar, and is captured in conventional FFT-based Doppler processing. However, the person's tangential velocity falls along *double-bounce* paths that scatter *twice* due to the pillar: radar → person → pillar → radar and radar → pillar →

Received 22 October 2024; revised 27 April 2025; accepted 19 July 2025. Date of publication 30 July 2025; date of current version 13 August 2025. This work was supported by NSF under Grant CNS-2215082 and Grant CNS-2215646. An earlier version of this paper was presented in part at the 2024 IEEE/NIST Conference on Computational Imaging Using Synthetic Apertures [DOI: 10.1109/CISA60639.2024.10576593]. The associate editor coordinating the review of this article and approving it for publication was Shobha Ram. *(Corresponding author: Nishant Mehrotra.)*

Nishant Mehrotra was with the Department of Electrical and Computer Engineering, Rice University, Houston, TX 77005 USA. He is now with the Department of Electrical and Computer Engineering, Duke University, Durham, NC 27708 USA (e-mail: nm370@duke.edu).

Divyanshu Pandey and Ashutosh Sabharwal are with the Department of Electrical and Computer Engineering, Rice University, Houston, TX 77005 USA (e-mail: dp76@rice.edu; ashu@rice.edu).

Upamanyu Madhow and Yasamin Mostofi are with the Department of Electrical and Computer Engineering, University of California, Santa Barbara, CA 93106 USA (e-mail: madhow@ece.ucsb.edu; ymostofi@ece.ucsb.edu).

This article has supplementary downloadable material available at https://doi.org/10.1109/TCI.2025.3594013, provided by the authors.

Digital Object Identifier 10.1109/TCI.2025.3594013

[1] By MIMO radars, we refer to radars with multiple transmit and receive antennas co-located on the same device, and not distributed radars with transmitters & receivers distributed across a wide geographical region.

[2] We follow the convention in automotive radar with a frame comprising between 64 to 256 chirps in a duration of the order of 10 ms [7], [8].

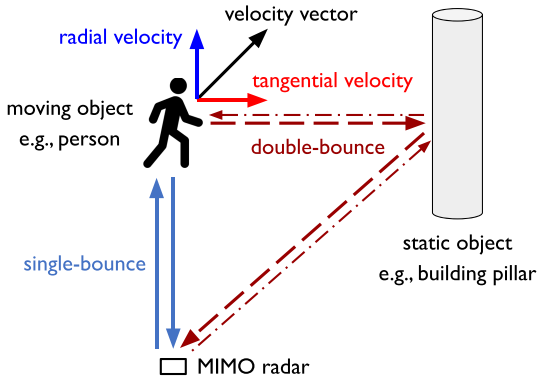

Fig. 1. Illustration of velocity vector estimation of a moving person via multi-bounce from a static building pillar. Two double-bounce paths are shown: radar → person → pillar → radar (dashed maroon line) and radar → pillar → person → radar (dash-dotted maroon line).

person → radar. Hence, fusing the LOS and double-bounce paths enables capturing multiple "looks" of the same moving object's velocity vector with a *single* MIMO radar - thus reducing the overall system cost and removing the need for multi-module synchronization. Our proposed approach is inspired by our prior analytical work [9] which showed theoretical radar imaging resolution gains on leveraging double-bounce scattering in addition to LOS paths.

The key idea behind our proposed radar signal processing scheme is to perform Doppler processing along both LOS and multi-bounce paths, as illustrated in Fig. 1. For simplicity, the scheme is restricted to 2D (range-azimuth) spatial processing. A preliminary version for a single moving point object with one static reflector was introduced in [1]. This work generalizes it to arbitrary extended objects and beyond double-bounce to include triple-bounce paths. We address two major challenges: (i) extracting single- and multi-bounce Doppler components when bounce locations are unknown, and (ii) extracting weak multi-bounce signals due to power decay [10]. To address the first challenge, we pre-map static objects and propose a multi-stage algorithm. The proposed algorithm initially maps moving objects and estimates single-bounce Doppler velocities. Then, it identifies background reflection points and estimates Doppler velocities along multi-bounce paths. Finally, it estimates object velocity vectors based on a custom clustering algorithm. The second challenge is addressed by sequentially processing Doppler signals – starting with higher-power lower-order bounces—to isolate and extract higher-order components.

We also present a detailed theoretical analysis to understand the benefits and limitations of our proposed scheme. We first derive fundamental limits for velocity vector estimation using single- and double-bounce scattering in an environment with two point objects, as a function of different system parameters via the geometric dilution-of-precision (DoP) [11] and the Cramér-Rao bound (CRB). We show that the geometrical configurations where the radar and the two objects form an approximate right triangle are most preferable from velocity estimation standpoint. In the Supplementary Material, the analysis is generalized to extended multiple objects - both static and moving. We also extend the analysis to triple-bounce scenarios. We show that when single- and double-bounce paths already exist, triple-bounce paths from the same point providing a double-bounce path does not add additional information and does not improve velocity vector estimation. However, in around-corner scenarios [12] with occluded single-bounce paths or scenarios with extended objects where points resulting in double-bounce and triple-bounce paths may be different, triple-bounce is beneficial for velocity vector estimation.

Finally, we extensively evaluate the performance of our method using an open source experimental radar dataset from Mercedes-Benz [13]. We utilize the dataset to evaluate the performance of our proposed pipeline that fuses single- and multi-bounce Doppler frequencies to estimate moving object's velocity vectors. We demonstrate that utilizing double-bounce paths improves the median velocity vector estimation error by $4.5\times$ over single-bounce baselines. We further use the dataset to validate the insights gained from our theoretical analysis.

To summarize, our contributions can be listed as follows:

- We propose a novel NLOS radar signal processing scheme that leverages multi-bounce scattering from static objects to estimate velocity vectors of moving objects within a single radar frame, while using only a single MIMO radar module.
- We theoretically analyze the estimation performance of the proposed scheme using DoP and CRB, and highlight different geometric and environmental characteristics that can affect the performance of our proposed algorithm.
- The proposed algorithm is evaluated on a real-world data set, validating the theoretical analysis and showing an improvement in performance when compared to baselines.

B. Comparison With Prior Work

To the best of our knowledge, our proposed approach of using multi-bounce for velocity vector estimation is novel and has not appeared previously. Most existing solutions that estimate the velocity vectors leverage additional degrees-of-freedom by tracking across multiple radar frames or deploying multiple hardware modules. Below, we survey such closely related prior work and outline differences with our approach.

Multi-frame object tracking: Standard approaches track objects across multiple radar frames [14], [15], [16]; however these methods require at least 2 (and up to 10) frames to converge to reliable estimates [17], hence can not provide single-frame velocity vector estimates in any given radar frame. While our work explores the complementary problem of single-frame velocity vector estimation, the proposed methods in this paper can also be used to improve multi-frame tracking algorithms.

Single-frame velocity vector estimation: Single-frame velocity estimation can be achieved by deploying multiple modules to capture different perspectives about the same moving objects, e.g., by deploying multiple synchronized radars [18], [19], [20], [21], [22], [23], [24], using a radar and multiple repeater elements [25] or fusing measurements from a co-located radar and

camera [6]. In contrast, our approach uses a *single* MIMO radar, thus reducing the overall system cost and removing the need for multi-module synchronization. Comparable single-radar solutions in the literature [26], [27], [28] fuse single-bounce radial velocity estimates of multiple points on a given object's surface. However, such methods fail when either the object has small physical extent, or the object is located at boresight to the radar and is moving tangentially. Our proposed method overcomes both these limitations. We benchmark our method against the single-radar methods in [26], [27], [28], and our evaluation in Section V shows $4.5\times$ improvement in the median velocity vector estimation error over the baselines.

Multi-bounce scattering: Multi-bounce scattering is often viewed as a nuisance due to the false detections, a.k.a. "ghosts" [13], [29], [30], [31], [32], [33], at physically incorrect locations with LOS radar processing. Instead, in this work, we view multi-bounce as an opportunity to improve existing radar pipelines. Prior work focuses on identifying "ghosts", and either suppressing them to improve object detection [13], [29], [30], [31], [32], [34], or remapping them to their ground truth locations for around-corner object localization [35], [36] and imaging [12], [37], [38], [39], [40], [41], [42], [43]. Further, multi-bounce scattering has been used to improve direction-of-arrival estimation [44], static object localization [21], [45], [46], [47], [48], static environment imaging [49], [50], [51], object tracking [52], [53], [54], [55] and radar metereology [56]. To the best of our knowledge, no prior work has harnessed multi-bounce scattering for velocity vector estimation.

C. Paper Outline

This paper is organized as follows. In Section II-B, we formulate the problem of velocity vector estimation with a single MIMO radar via multi-bounce scattering. We then develop our proposed approach in Section III. We theoretically analyze our algorithm in Section IV, and present experimental evaluation in Section V. We conclude the paper in Section VI with some discussions and directions for future work.

D. Notation & Basic Definitions

We use bold uppercase for matrices (e.g., $\mathbf{X}$), bold lowercase for vectors (e.g., $\mathbf{x}$) and non-bold lowercase for scalars (e.g., x). Sets are represented using calligraphic fonts (e.g., $\mathcal{X}$), with cardinality $|\mathcal{X}|$. The Kronecker product is denoted by $\otimes$. The transpose, complex conjugate, and Hermitian operators are denoted by $(\cdot)^\top$, $(\cdot)^*$ and $(\cdot)^\mathsf{H}$. Symbol $\mathbb{E}$ denotes expectation, O denotes big-O (order of) notation, and $\mathbf{A} \succeq \mathbf{B}$ indicates that the matrix $(\mathbf{A}-\mathbf{B})$ is positive semidefinite. The $n \times n$ identity matrix and $n \times m$ all-zeros matrix are denoted by $\mathbf{I}_{n\times n}$ and $\mathbf{0}_{n\times m}$. The (n,m)th entry of a matrix $\mathbf{X}$ is denoted by $[\mathbf{X}]_{n,m}$, and the ith entry of a vector $\mathbf{x}$ is denoted by $[\mathbf{x}]_i$. The trace of a matrix $\mathbf{X}$ is denoted by $\mathsf{Tr}[\mathbf{X}]$. The p-norm of a vector $\mathbf{x}$ is denoted by $\|\mathbf{x}\|_p$, and the inner product of two vectors $\mathbf{x}$ and $\mathbf{y}$ is $\langle \mathbf{x}, \mathbf{y}\rangle$. The real and imaginary parts of a complex scalar x are denoted by $\mathsf{Re}\{x\}$ and $\mathsf{Im}\{x\}$. The gradient of a scalar function $a(\boldsymbol{\theta})$ with respect to an $n \times 1$ vector parameter $\boldsymbol{\theta}$ is defined as the $n \times 1$ vector:

$$\left(\frac{\partial a(\boldsymbol{\theta})}{\partial \boldsymbol{\theta}}\right) \triangleq \left[\frac{\partial a(\boldsymbol{\theta})}{\partial [\boldsymbol{\theta}]_1} \frac{\partial a(\boldsymbol{\theta})}{\partial [\boldsymbol{\theta}]_2} \cdots \frac{\partial a(\boldsymbol{\theta})}{\partial [\boldsymbol{\theta}]_n}\right]^\top.$$

The gradient of an $m \times 1$ vector-valued function $\mathbf{a}(\boldsymbol{\theta})$ with respect to $n \times 1$ vector $\boldsymbol{\theta}$ is defined as the $n \times m$ matrix:

$$\left(\frac{\partial \mathbf{a}(\boldsymbol{\theta})}{\partial \boldsymbol{\theta}}\right) \triangleq \left[\frac{\partial [\mathbf{a}(\boldsymbol{\theta})]_1}{\partial \boldsymbol{\theta}} \frac{\partial [\mathbf{a}(\boldsymbol{\theta})]_2}{\partial \boldsymbol{\theta}} \cdots \frac{\partial [\mathbf{a}(\boldsymbol{\theta})]_m}{\partial \boldsymbol{\theta}}\right].$$

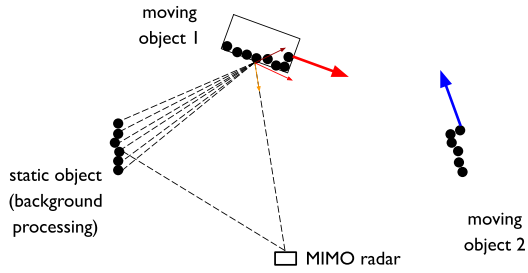

Fig. 2. Example system configuration with a MIMO radar estimating the velocity vectors of two extended moving objects in the presence of an extended static object.

II. Problem Formulation

The goal of this work is to estimate the full-velocity vectors of moving objects with a single MIMO radar by exploiting multi-bounce scattering from secondary static objects in the environment. An exemplary 2D diagram of the considered setting is shown in Fig. 2 with two extended moving objects and an extended static object near a MIMO radar. We consider a single radar frame duration with multiple frequency-modulated continuous wave (FMCW) chirp transmissions. Our problem is formulated under the following assumptions:

Assumption 1 (Static Radar): For simplicity, we assume the radar is static and only objects in the environment move. However, our proposed method can be used to estimate the velocity vectors of moving objects relative to the radar when the radar is also moving (e.g., when mounted on a vehicle).

Assumption 2 (2D Processing): We restrict all processing to the 2D range-azimuth plane relative to the radar, which is reasonable for terrestrial navigation use-cases where all motion occurs on the 2D road surface. However, this assumption is not critical and can be extended to 3D objects by incorporating elevation angles in the model and algorithms.

Assumption 3 (Far-Field Regime): We assume all objects in the environment are in the far-field to the radar, i.e., are located beyond the Fraunhoufer distance [57] of the radar antenna array. This assumption is easily satisfied in practice. For instance, for the 77 GHz radar sensors used in our evaluation dataset [13], the Fraunhoufer distance is approximately 2 m, with all objects at 5 m or beyond from the radar.

Assumption 4 (Small Time-Bandwidth Product): We assume the radar's time-bandwidth product is small enough to neglect Doppler variation within a single radar chirp and assume frequency-flat array steering vectors.

Assumption 5 (Non-Rotating Rigid Bodies): We assume every moving object is a non-rotating rigid body, whose motion at time snapshot t is modeled by a 2D velocity vector $\mathbf{v}(t)$, which is the same for all points on the object surface.

Assumption 6 (Background Subtraction): Given the radar is assumed to remain static (Assumption 1), we assume the radar has a one-shot estimate of static objects in the environment (background). In subsequent frames with moving objects, LOS scattering from static objects is cancelled by subtracting the radar data collected in the presence and absence of moving objects. We note that this assumption is not critical to our proposed approach in Section III, and is only made to simplify the problem formulation and algorithm description. Velocity vector estimation can be performed jointly with background mapping, e.g., via methods proposed by the authors in [48].

Assumption 7 (Negligible Intra-Object Multi-Bounce): We neglect multi-bounce scattering between points belonging to the same object since such paths cannot provide any extra information about the object's motion given all points on the object have the same velocity vector as per Assumption 5.

Assumption 8 (Omni-Directional Scattering): We assume that all objects in the environment scatter incident radiation omni-directionally, independent of the incident angle. This assumption simplifies the system model and algorithm design, however does not limit applicability; in Section V we demonstrate good performance even with specular reflecting surfaces like metallic doors and marble walls.

Note: The above assumptions are made for ease of exposition and do not limit practical applicability of our algorithm. Assumptions 3, 4, 5, 7, and 8 are standard in the automotive radar literature, e.g., see [12], [48], [58], and do not limit real-world practical applicability, as is evidenced by practical demonstration of the proposed algorithm in Section V across a wide variety of real-world outdoor environments. Assumptions 1, 2, and 6 are made to simplify algorithm development, and can be relaxed in practice as described previously.

With the above assumptions, we now describe the system model and formulate the problem of full-velocity estimation.

A. System Model

We describe the system model in two stages. First, we develop a Doppler model for multi-bounce paths, which forms the core component of our overall system model. Then, we formulate the actual signal model for the radar's measurements.

1) Multi-Bounce Doppler Model: Consider an n-bounce path where the signal transmitted by the radar bounces at n objects before being received back at the radar: radar $\rightarrow$ object 1 $\rightarrow$ object 2 $\rightarrow \cdots \rightarrow$ object $n \rightarrow$ radar, as shown in Fig. 3. Let $\mathbf{v}_i$ and $\mathbf{r}_i$ respectively denote the 2D velocity and position vectors of the ith object at the radar frame of interest, where the dependence on the frame instance is suppressed for notational clarity. Let $\hat{\mathbf{k}}_i = \frac{\mathbf{r}_{i+1}-\mathbf{r}_i}{\|\mathbf{r}_{i+1}-\mathbf{r}_i\|_2}$, $\forall i \in \{0, 1, \ldots, n\}$ denote the unit vector pointing from the ith to the $(i+1)$th objects, where $\mathbf{r}_0 = \mathbf{r}_{n+1}$ denotes the radar's position. Then,

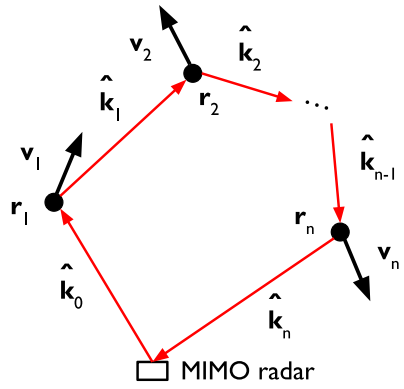

Fig. 3. n-bounce Doppler modeling.

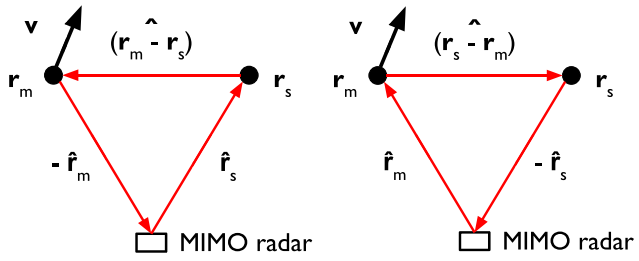

(a) Type-I paths. (b) Type-II paths.

Fig. 4. Modeling double-bounce paths.

the Doppler frequency along the n-bounce path is [59], [60][3]

$$\mathrm{f}_n = \frac{1}{\lambda}\sum_{i=1}^{n}\left\langle \hat{\mathbf{k}}_i - \hat{\mathbf{k}}_{i-1}, \mathbf{v}_i \right\rangle, \tag{1}$$

where λ denotes the wavelength at the carrier frequency.

Special Case 1 (Single-Bounce): In the specific case of single-bounce scattering: radar $\rightarrow$ object $\rightarrow$ radar, (1) reduces to the well-known Doppler relation $\mathrm{f}_1 = \frac{-2}{\lambda_c}\left\langle \frac{\mathbf{r}}{\|\mathbf{r}\|_2}, \mathbf{v} \right\rangle$, assuming the radar is at the origin of the coordinate system.

Special Case 2 (Double-Bounce): In the case of double-bounce scattering from a static secondary reflector, two paths are possible as shown in Fig. 4: radar $\rightarrow$ object $\rightarrow$ reflector $\rightarrow$ radar or radar $\rightarrow$ reflector $\rightarrow$ object $\rightarrow$ radar. For both paths, (1) reduces to the same Doppler relation $\mathrm{f}_2 = \frac{-1}{\lambda_c}\left\langle \frac{\mathbf{r}_\mathrm{m}}{\|\mathbf{r}_\mathrm{m}\|_2} + \frac{\mathbf{r}_\mathrm{m}-\mathbf{r}_\mathrm{s}}{\|\mathbf{r}_\mathrm{m}-\mathbf{r}_\mathrm{s}\|_2}, \mathbf{v} \right\rangle$, where $\mathbf{r}_\mathrm{m}$ and $\mathbf{r}_\mathrm{s}$ respectively denote the moving object's and static reflector's 2D location.

Special Case 3 (Triple-Bounce): For triple-bounce scattering from a static reflector along type-I paths shown in Fig. 5(a): radar $\rightarrow$ object $\rightarrow$ reflector $\rightarrow$ object $\rightarrow$ radar, (1) reduces to $\mathrm{f}_{3,\mathrm{I}} = \frac{-2}{\lambda_c}\left\langle \frac{\mathbf{r}_\mathrm{m}}{\|\mathbf{r}_\mathrm{m}\|_2} + \frac{\mathbf{r}_\mathrm{m}-\mathbf{r}_\mathrm{s}}{\|\mathbf{r}_\mathrm{m}-\mathbf{r}_\mathrm{s}\|_2}, \mathbf{v} \right\rangle$, where $\mathbf{r}_\mathrm{m}$ and $\mathbf{r}_\mathrm{s}$ respectively denote the moving object's and static reflector's 2D location vectors. Along type-II paths shown in Fig. 5(b): radar $\rightarrow$ reflector $\rightarrow$ object $\rightarrow$ reflector $\rightarrow$ radar, (1) reduces to $\mathrm{f}_{3,\mathrm{II}} = \frac{-2}{\lambda_c}\left\langle \frac{\mathbf{r}_\mathrm{m}-\mathbf{r}_\mathrm{s}}{\|\mathbf{r}_\mathrm{m}-\mathbf{r}_\mathrm{s}\|_2}, \mathbf{v} \right\rangle$. We note that more general triple-bounce scenarios are possible, e.g., with reflections from 1 moving and 2 static objects, that have been utilized in previous work by the authors [48] for beyond-field-of-view static object localization.

[3]Also see Supplementary Material for a derivation of (1).

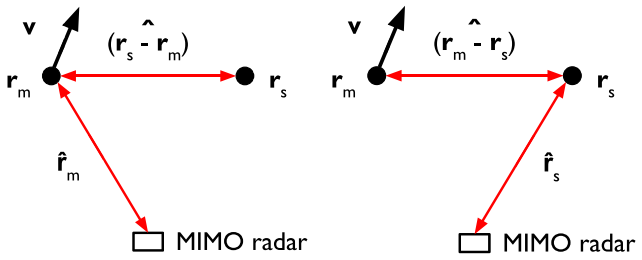

(a) Type-I paths. (b) Type-II paths.

Fig. 5. Modeling triple-bounce paths.

We do not consider such cases in this paper since such general triple-bounce scenarios do not appear in the dataset [13] used in our evaluation, and extensions to such scenarios are left for future work.

We now formulate the radar's signal/measurement model.

2) Radar Signal Model: We assume M moving extended objects and N static extended objects within the radar's field-of-view. Each moving object is assumed to move with velocity vector $\mathbf{v}_m$ and comprises P_m, $m \in \{1, \ldots, \mathsf{M}\}$ point reflectors, whose locations and velocity vectors are unknown to the radar. Similarly, each static object comprises P_n, $n \in \{1, \ldots, \mathsf{N}\}$ point reflectors, whose locations are known to the radar as per Assumption 6. As per Assumptions 6 and 7, we do not model single-bounce scattering from static objects and do not model intra-object multi-bounce.

We model the MIMO radar as a T-antenna transmit array and a R-antenna receive array. Within a single radar frame, the radar transmits L FMCW chirps, of starting frequency f_c and duration T_c, in a time-orthogonal fashion across all T antennas with a per-antenna transmit power P_{TX}. The radar receiver mixes the reflected chirps with the transmitted chirps, and the resultant $\mathsf{TR} \times 1$ vector of "dechirped" signals, for FMCW instantaneous frequency ω and chirp index ℓ, is

$$\mathbf{y}(\omega;\ell) = \sqrt{\mathsf{P}_{\mathsf{TX}}} \sum_{m=1}^{\mathsf{M}} \Bigg[\mathbf{y}_1^m(\omega;\ell) + \sum_{n=1}^{\mathsf{N}} \Big(\mathbf{y}_2^{m,n}(\omega;\ell) + \mathbf{y}_{3,\mathsf{I}}^{m,n}(\omega;\ell) + \mathbf{y}_{3,\mathsf{II}}^{m,n}(\omega;\ell) \Big) \Bigg] + \mathbf{y}_{\mathsf{r}}(\omega;\ell) + \mathbf{n}, \tag{2}$$

where subscript n, t indicates n-bounce paths of type-t, $\mathbf{y}_{\mathsf{r}}(\omega;\ell)$ denotes residual multi-bounce terms, e.g., due to incorrect background subtraction, and $\mathbf{n}$ denotes complex additive Gaussian noise of identity covariance. The terms $\mathbf{y}_1^m(\omega;\ell)$, $\mathbf{y}_2^{m,n}(\omega;\ell)$, $\mathbf{y}_{3,\mathsf{I}}^{m,n}(\omega;\ell)$, $\mathbf{y}_{3,\mathsf{II}}^{m,n}(\omega;\ell)$ are:

$$\mathbf{y}_1^m(\omega;\ell) = \sum_{p_m=1}^{\mathsf{P}_m} \mathbf{y}_1^{p_m}(\omega) e^{j2\pi \mathsf{f}_1(\mathbf{v}_m;p_m)\ell \mathsf{T}_c}, \tag{3}$$

$$\mathbf{y}_2^{m,n}(\omega;\ell) = \sum_{p_m=1}^{\mathsf{P}_m} \sum_{p_n=1}^{\mathsf{P}_n} \mathbf{y}_2^{p_m;p_n}(\omega) e^{j2\pi \mathsf{f}_2(\mathbf{v}_m;p_m;p_n)\ell \mathsf{T}_c}, \tag{4}$$

$$\mathbf{y}_{3,\mathsf{I}}^{m,n}(\omega;\ell) = \sum_{p_m=1}^{\mathsf{P}_m} \sum_{p_n=1}^{\mathsf{P}_n} \mathbf{y}_{3,\mathsf{I}}^{p_m;p_n}(\omega) e^{j2\pi \mathsf{f}_{3,\mathsf{I}}(\mathbf{v}_m;p_m;p_n)\ell \mathsf{T}_c}, \tag{5}$$

$$\mathbf{y}_{3,\mathsf{II}}^{m,n}(\omega;\ell) = \sum_{p_m=1}^{\mathsf{P}_m} \sum_{p_n=1}^{\mathsf{P}_n} \mathbf{y}_{3,\mathsf{II}}^{p_m;p_n}(\omega) e^{j2\pi \mathsf{f}_{3,\mathsf{II}}(\mathbf{v}_m;p_m;p_n)\ell \mathsf{T}_c}. \tag{6}$$

Variables $\mathsf{f}_1(\mathbf{v}_m;p_m)$, $\mathsf{f}_2(\mathbf{v}_m;p_m;p_n)$, $\mathsf{f}_{3,\mathsf{I}}(\mathbf{v}_m;p_m;p_n)$, $\mathsf{f}_{3,\mathsf{II}}(\mathbf{v}_m;p_m;p_n)$ in (3)–(6) denote Doppler terms, which are defined based on (1) and Special Cases 1-3:

$$\mathsf{f}_1(\mathbf{v}_m;p_m) = \frac{-2}{\lambda_c} \left\langle \frac{\mathbf{r}_{p_m}}{\|\mathbf{r}_{p_m}\|_2}, \mathbf{v}_m \right\rangle, \tag{7}$$

$$\mathsf{f}_2(\mathbf{v}_m;p_m;p_n) = \frac{-1}{\lambda_c} \left\langle \frac{\mathbf{r}_{p_m}}{\|\mathbf{r}_{p_m}\|_2} + \frac{\mathbf{r}_{p_m} - \mathbf{r}_{p_n}}{\|\mathbf{r}_{p_m} - \mathbf{r}_{p_n}\|_2}, \mathbf{v}_m \right\rangle, \tag{8}$$

$$\mathsf{f}_{3,\mathsf{I}}(\mathbf{v}_m;p_m;p_n) = \frac{-2}{\lambda_c} \left\langle \frac{\mathbf{r}_{p_m}}{\|\mathbf{r}_{p_m}\|_2} + \frac{\mathbf{r}_{p_m} - \mathbf{r}_{p_n}}{\|\mathbf{r}_{p_m} - \mathbf{r}_{p_n}\|_2}, \mathbf{v}_m \right\rangle, \tag{9}$$

$$\mathsf{f}_{3,\mathsf{II}}(\mathbf{v}_m;p_m;p_n) = \frac{-2}{\lambda_c} \left\langle \frac{\mathbf{r}_{p_m} - \mathbf{r}_{p_n}}{\|\mathbf{r}_{p_m} - \mathbf{r}_{p_n}\|_2}, \mathbf{v}_m \right\rangle. \tag{10}$$

Note that in (7)–(10), wavelength $\lambda_c = \frac{\mathsf{c}}{\mathsf{f}_c}$ is defined for the FMCW starting frequency f_c, where c denotes speed of light.

Variables $\mathbf{y}_1^{p_m}(\omega)$, $\mathbf{y}_2^{p_m;p_n}(\omega)$, $\mathbf{y}_{3,\mathsf{I}}^{p_m;p_n}(\omega)$, $\mathbf{y}_{3,\mathsf{II}}^{p_m;p_n}(\omega)$ in (3)–(6) represent Doppler-independent factors due to scattering from objects along the multi-bounce paths, and are defined based on Assumption 4. The single-bounce term $\mathbf{y}_1^{p_m}(\omega)$ is

$$\mathbf{y}_1^{p_m}(\omega) = \sigma_{p_m} \left(\mathbf{a}_{\mathsf{RX}}(\theta_{p_m}) \otimes \mathbf{a}_{\mathsf{TX}}(\theta_{p_m}) \right) \frac{e^{-j\frac{\omega}{\mathsf{c}}\mathsf{d}_1^{p_m}}}{4\pi^2 (\mathsf{d}_1^{p_m})^2}, \tag{11}$$

where σ_{p_m} denotes the reflectivity of the point object p_m, $\mathbf{a}_{\mathsf{TX/RX}}(\theta_{p_m})$ denotes the (frequency-flat) $\mathsf{T} \times 1$ transmit or $\mathsf{R} \times 1$ receive steering vector for azimuth angle θ_{p_m} corresponding to p_m, and $\mathsf{d}_1^{p_m} = 2\|\mathbf{r}_{p_m}\|_2$ is the round-trip length of the single-bounce path from the radar to p_m.

Similarly, the double-bounce term $\mathbf{y}_2^{p_m;p_n}(\omega)$ is defined as

$$\mathbf{y}_2^{p_m;p_n}(\omega) = \sigma_{p_m}\sigma_{p_n} \left[\mathbf{a}_{\mathsf{RX}}(\theta_{p_m}) \otimes \mathbf{a}_{\mathsf{TX}}(\theta_{p_n}) + \mathbf{a}_{\mathsf{RX}}(\theta_{p_n}) \otimes \mathbf{a}_{\mathsf{TX}}(\theta_{p_m}) \right] \frac{e^{-j\frac{\omega}{\mathsf{c}}\mathsf{d}_2^{p_m;p_n}}}{4\pi^2 (\mathsf{d}_2^{p_m;p_n})^2}, \tag{12}$$

corresponding to both types of paths shown in Fig. 4, where the radar transmits towards either p_m or p_n and receives reflections from the other object. The term $\mathsf{d}_2^{p_m;p_n} = \|\mathbf{r}_{p_m}\|_2 + \|\mathbf{r}_{p_m} - \mathbf{r}_{p_n}\|_2 + \|\mathbf{r}_{p_n}\|_2$ denotes the total length of either of the two possible double-bounce paths.

The type-I triple-bounce term $\mathbf{y}_{3,\mathsf{I}}^{p_m;p_n}(\omega)$ is given as

$$\mathbf{y}_{3,\mathsf{I}}^{p_m;p_n}(\omega) = \sigma_{p_m;p_n}^{\mathsf{TB,I}} \left(\mathbf{a}_{\mathsf{RX}}(\theta_{p_m}) \otimes \mathbf{a}_{\mathsf{TX}}(\theta_{p_m}) \right) \frac{e^{-j\frac{\omega}{\mathsf{c}}\mathsf{d}_{3,\mathsf{I}}^{p_m;p_n}}}{4\pi^2 (\mathsf{d}_{3,\mathsf{I}}^{p_m;p_n})^2}, \tag{13}$$

where $\mathsf{d}_{3,\mathsf{I}}^{p_m;p_n} = 2\|\mathbf{r}_{p_m}\|_2 + 2\|\mathbf{r}_{p_m} - \mathbf{r}_{p_n}\|_2$ is the total length and $\sigma_{p_m;p_n}^{\mathsf{TB,I}} = \sigma_{p_m}^2 \sigma_{p_n}$ is the reflectivity of the path that bounces twice at p_m and once at p_n. Similarly, the type-II triple-bounce

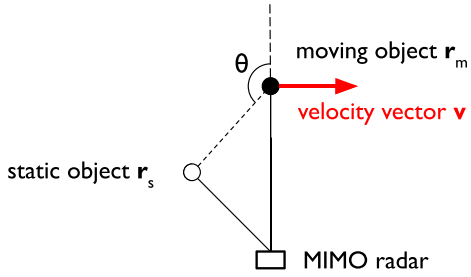

Fig. 6. Toy example with two point objects.

term $\mathbf{y}_{3,\mathsf{II}}^{p_m;p_n}(\omega)$ is

$$\mathbf{y}_{3,\mathsf{II}}^{p_m;p_n}(\omega) = \sigma_{p_m;p_n}^{\mathsf{TB,II}} \left(\mathbf{a}_{\mathsf{RX}}(\theta_{p_n}) \otimes \mathbf{a}_{\mathsf{TX}}(\theta_{p_n})\right) \frac{e^{-j\frac{\omega}{c}\mathsf{d}_{3,\mathsf{II}}^{p_m;p_n}}}{4\pi^2 (\mathsf{d}_{3,\mathsf{II}}^{p_m;p_n})^2}, \quad (14)$$

where $\mathsf{d}_{3,\mathsf{II}}^{p_m;p_n} = 2\|\mathbf{r}_{p_n}\|_2 + 2\|\mathbf{r}_{p_m} - \mathbf{r}_{p_n}\|_2$ is the total length and $\sigma_{p_m;p_n}^{\mathsf{TB,II}} = \sigma_{p_m}\sigma_{p_n}^2$ is the reflectivity of the path that bounces twice at p_n and once at p_m.

Finally, $\mathbf{y}_{\mathsf{r}}(\omega;\ell)$ corresponds to residual multi-bounce terms, e.g., double-bounce or triple-bounce scattering between moving objects, fourth-bounce and higher-order bounces, inter-object multi-bounce terms, etc. While we do not explicitly account for such terms in our proposed approach in Section III, we evaluate their impact theoretically in Section IV and experimentally in Section V.

B. Problem Statement

Given the system model in (2), our aim in this paper is to estimate the 2D velocity vectors $\mathbf{v}_m$ of all moving objects $m \in \{1,\ldots,\mathsf{M}\}$, while also estimating the 2D locations $\mathbf{r}_{p_m}$ of points p_m belonging to each object m. The optimization problem can be stated as:

$$\min_{\{\mathbf{r}_{p_m},\mathbf{v}_m\}} \frac{1}{\mathsf{LW}} \sum_{\ell=1}^{\mathsf{L}} \sum_{\omega=1}^{\mathsf{W}} \Bigg\| \mathbf{y}(\omega;\ell) - \sqrt{\mathsf{P}_{\mathsf{TX}}} \sum_{m=1}^{\mathsf{M}} \Bigg[\mathbf{y}_1^m(\omega;\ell) + \sum_{n=1}^{\mathsf{N}} \left(\mathbf{y}_2^{m,n}(\omega;\ell) + \mathbf{y}_{3,\mathsf{I}}^{m,n}(\omega;\ell) + \mathbf{y}_{3,\mathsf{II}}^{m,n}(\omega;\ell) \right) \Bigg] \Bigg\|_2^2. \quad (\mathrm{P})$$

III. Proposed Approach

We present our approach in a step-by-step fashion. We begin by illustrating the key ideas underlying our approach in Section III-A for a simple "toy" example shown in Fig. 6 with two point objects, one moving and the other static. We then describe our approach in its full generality in Section III-B.

A. Toy Example: One Point-Like Static & Moving Object

The overall idea of our approach can be illustrated via a simple example shown in Fig. 6 with $\mathsf{M} = 1$ moving point object with velocity vector $\mathbf{v}$ and location $\mathbf{r}_m$, and $\mathsf{N} = 1$ static point object located at $\mathbf{r}_s$. Assume for the time being that locations $\mathbf{r}_m$, $\mathbf{r}_s$ and all Doppler terms in (7)–(10) are known to the radar, and the only unknown is the moving object's velocity vector $\mathbf{v}$. Adapting the definitions of the Doppler terms from (7)–(10) to this setting, it

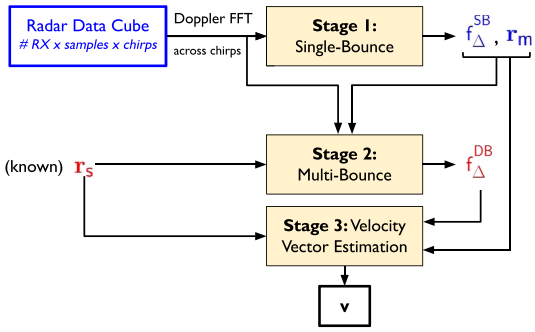

Fig. 7. Algorithm flow for toy example in Fig. 6.

is easy to see that $\mathbf{v}$ can be estimated by solving the following least-squares problem:

$$\mathbf{v} = \arg\min_{\mathbf{w}} \left\| \begin{bmatrix} \mathsf{f}_1 \\ \mathsf{f}_2 \\ \mathsf{f}_{3,\mathsf{I}} \\ \mathsf{f}_{3,\mathsf{II}} \end{bmatrix} + \frac{1}{\lambda_c} \begin{bmatrix} \frac{2\mathbf{r}_m^\top}{\|\mathbf{r}_m\|_2} \\ \frac{\mathbf{r}_m^\top}{\|\mathbf{r}_m\|_2} + \frac{(\mathbf{r}_m - \mathbf{r}_s)^\top}{\|\mathbf{r}_m - \mathbf{r}_s\|_2} \\ \frac{2\mathbf{r}_m^\top}{\|\mathbf{r}_m\|_2} + \frac{2(\mathbf{r}_m - \mathbf{r}_s)^\top}{\|\mathbf{r}_m - \mathbf{r}_s\|_2} \\ \frac{2(\mathbf{r}_m - \mathbf{r}_s)^\top}{\|\mathbf{r}_m - \mathbf{r}_s\|_2} \end{bmatrix} \mathbf{w} \right\|_2^2. \quad (15)$$

Overall Algorithm Flow: The overall idea of our approach is to separately estimate the multi-bounce Doppler terms f_1, f_2, $\mathsf{f}_{3,\mathsf{I}}$, $\mathsf{f}_{3,\mathsf{II}}$ and moving object location $\mathbf{r}_m$, then solve the least squares problem in (15), assuming the static object's location $\mathbf{r}_s$ is known to the radar as per Assumption 5. The algorithm proceeds in three stages as shown in Fig. 7.

Stage 1 (Single-Bounce): In the first stage, the radar treats all multi-bounce terms of higher order than single-bounce as noise, and employs conventional single-bounce processing to estimate the moving object's location $\mathbf{r}_m$ and the single-bounce Doppler term f_1 . Such an assumption is feasible since it is well-known that the received signal power decays (typically by over 20dB) with each increasing bounce [10], [61]. The particular processing steps are as follows. Assuming the environment around the radar is discretized into a 2D grid of point object locations (indexed by grid locations $\mathbf{p}$), the radar solves the following least-squares problem:

$$(\mathsf{f}_1, \mathbf{r}_m) = \arg\min_{\mathsf{f},\mathbf{p}} \frac{1}{\mathsf{LW}} \sum_{\ell=1}^{\mathsf{L}} \sum_{\omega=1}^{\mathsf{W}} \left\| \mathbf{y}(\omega;\ell) - \mathbf{y}_1^{\mathsf{P}}(\omega) e^{j2\pi \mathsf{f} \ell \mathsf{T}_c} \right\|_2^2,$$

where $\mathbf{y}_1^{\mathsf{P}}(\omega)$ is defined similar to (11) for a hypothetical grid location $\mathbf{p}$ with unit reflectivity, i.e., $\sigma_{\mathsf{p}} = 1$. Under the mild assumption of unit-norm steering vectors (satisfied in practice), the above reduces to the following *matched filter* problem:

$$(\mathsf{f}_1, \mathbf{r}_m) = \arg\max_{\mathsf{f},\mathbf{p}} \frac{1}{\mathsf{W}} \sum_{\omega=1}^{\mathsf{W}} \mathsf{Re}\left\{ (\mathbf{y}_1^{\mathsf{P}}(\omega))^{\mathsf{H}} \mathcal{F}(\mathbf{y})(\omega;\mathsf{f}) \right\}, \quad (16)$$

where $\mathcal{F}(\mathbf{y})(\omega;\mathsf{f}) = \frac{1}{\mathsf{L}} \sum_{\ell=1}^{\mathsf{L}} \mathbf{y}(\omega;\ell) e^{-j2\pi \mathsf{f} \ell \mathsf{T}_c}$ denotes the Doppler FFT of the radar measurements $\mathbf{y}(\omega;\ell)$ taken over the transmitted chirps. By definition, the Doppler resolution is inversely proportional to L, the number of chirps per frame. From its definition in (11), the operation $(\mathbf{y}_1^{\mathsf{P}}(\omega))^{\mathsf{H}}$ can be understood as transmit and receive beamforming towards hypothetical grid locations $\mathbf{p}$, and compensating for the single-bounce path delay

to/from $\mathbf{p}$. The grid location $\mathbf{p}$ and Doppler bin f with the highest matched filter output magnitude yield the moving object's location $\mathbf{r}_\mathsf{m}$ and the corresponding single-bounce Doppler term f_1.

Stage 2 (Multi-Bounce): Having estimated the moving object's location $\mathbf{r}_\mathsf{m}$ and single-bounce Doppler term f_1, the radar next sequentially estimates the multi-bounce Doppler terms $\mathsf{f}_2, \mathsf{f}_{3,\mathsf{I}}, \mathsf{f}_{3,\mathsf{II}}$. Let $\mathbf{y}_{-1}(\omega;\ell) = \mathbf{y}(\omega;\ell) - \mathbf{y}_1^{\mathbf{r}_\mathsf{m}}(\omega)e^{j2\pi\mathsf{f}_1\ell\mathsf{T}_\mathsf{c}}$ denote the difference between the radar measurements and the estimated single-bounce terms. Equivalently, $\mathbf{y}_{-1}(\omega;\ell)$ denotes the residual double-bounce and higher order multi-bounce terms. To estimate the double-bounce Doppler term f_2, the following problem is solved:

$$\mathsf{f}_2 = \arg\min_{\mathsf{f}} \frac{1}{\mathsf{LW}} \sum_{\ell=1}^{\mathsf{L}} \sum_{\omega=1}^{\mathsf{W}} \left\| \mathbf{y}_{-1}(\omega;\ell) - \mathbf{y}_2^{\mathbf{r}_\mathsf{m};\mathbf{r}_\mathsf{s}}(\omega) e^{j2\pi\mathsf{f}\ell\mathsf{T}_\mathsf{c}} \right\|_2^2,$$

where $\mathbf{y}_2^{\mathbf{r}_\mathsf{m};\mathbf{r}_\mathsf{s}}(\omega)$ is defined similar to (12) with unit reflectivities, $\sigma_{\mathbf{r}_\mathsf{m}} = \sigma_{\mathbf{r}_\mathsf{s}} = 1$. The above problem reduces to a similar matched filter problem as in (16):

$$\mathsf{f}_2 = \arg\max_{\mathsf{f}} \frac{1}{\mathsf{W}} \sum_{\omega=1}^{\mathsf{W}} \mathsf{Re}\left\{ (\mathbf{y}_2^{\mathbf{r}_\mathsf{m};\mathbf{r}_\mathsf{s}}(\omega))^{\mathsf{H}} \mathcal{F}(\mathbf{y}_{-1})(\omega;\mathsf{f}) \right\}, \quad (17)$$

and corresponds to performing Doppler FFT on $\mathbf{y}_{-1}(\omega;\ell)$, i.e., *after removing* the estimated single-bounce components from the raw measurements $\mathbf{y}(\omega;\ell)$, followed by transmit beamforming towards the moving object $\mathbf{r}_\mathsf{m}$ and receive beamforming from the static object $\mathbf{r}_\mathsf{s}$. A similar procedure can be followed to estimate the triple-bounce Doppler terms $\mathsf{f}_{3,\mathsf{I}}$, $\mathsf{f}_{3,\mathsf{II}}$ as well as higher-order multi-bounce terms. We note that the above procedure is similar to successive interference cancellation [62, Chapter 6] in wireless systems and the CLEAN algorithm [63] in radar signal processing.

However, a potential drawback of the above procedure is that any residual errors due to imperfect cancellation at any stage may propagate to later stages and degrade Doppler estimation of higher-order bounces. Therefore, as an alternative, we propose to perform matched filtering *without removing* the single-bounce terms from the measurements $\mathbf{y}(\omega;\ell)$,

$$\mathsf{f}_2 = \arg\max_{\mathsf{f}} \frac{1}{\mathsf{W}} \sum_{\omega=1}^{\mathsf{W}} \mathsf{Re}\left\{ (\mathbf{y}_2^{\mathbf{r}_\mathsf{m};\mathbf{r}_\mathsf{s}}(\omega))^{\mathsf{H}} \mathcal{F}(\mathbf{y})(\omega;\mathsf{f}) \right\}, \quad (18)$$

which will be used in the remainder of this paper. In Section IV-A, we derive the specific conditions under which (17) can be simplified into (18).

Stage 3 (Full-Velocity Estimation): Finally, given estimates of the single-bounce and (at least one) higher-order multi-bounce Doppler terms, the least-squares problem in (15) is solved (with appropriate modifications). We analyze the impact of not estimating some terms in (15) later in Section IV-C.

B. General Case: Multiple Extended Objects

We now generalize the method from Section III-A to estimate the full-velocity vectors of multiple extended objects.

Overall Algorithm Flow: The overall algorithm flow is depicted in Fig. 8. The overall processing remains similar to the toy example from Section III-A, wherein the radar first performs single-bounce processing, followed by multi-bounce processing and a final velocity vector estimation stage, with appropriate clustering steps to associate radar detections to extended objects. The algorithm proceeds in four stages.

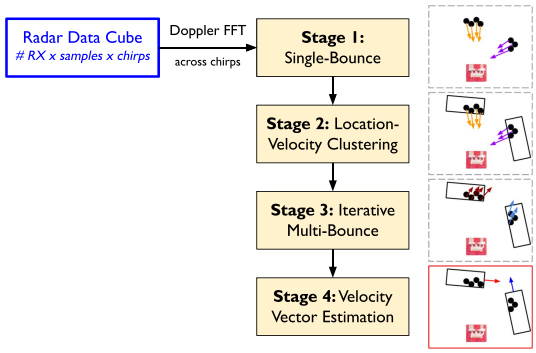

Fig. 8. Overall algorithmic flow of proposed method.

Stage 1 (Single-Bounce Point Clouds): To form point clouds of the surrounding environment, the radar first performs the matched filtering operation from (16) to estimate the reflectivities σ_p and Doppler frequencies $\mathsf{f}_1(\mathbf{p})$ of individual grid locations $\mathbf{p}$ in the environment:

$$\mathsf{f}_1(\mathbf{p}) = \arg\max_{\mathsf{f}} \frac{1}{\mathsf{W}} \sum_{\omega=1}^{\mathsf{W}} \mathsf{Re}\left\{ (\mathbf{y}_1^{\mathsf{p}}(\omega))^{\mathsf{H}} \mathcal{F}(\mathbf{y})(\omega;\mathsf{f}) \right\}, \quad (19)$$

$$\sigma_\mathsf{p} = \frac{1}{\mathsf{W}} \sum_{\omega=1}^{\mathsf{W}} \mathsf{Re}\left\{ (\mathbf{y}_1^{\mathsf{p}}(\omega))^{\mathsf{H}} \mathcal{F}(\mathbf{y})(\omega;\mathsf{f}_1(\mathbf{p})) \right\}. \quad (20)$$

The estimated reflectivities σ_p are then thresholded via an appropriate radar detector, e.g., CFAR [12], [64], [65], to estimate a point cloud $\mathcal{P}$ of the surrounding environment:

$$\mathcal{P} = \left\{ \mathbf{p} : \sigma_\mathsf{p} \geq \tau_{\mathsf{CFAR}} \right\}. \quad (21)$$

Stage 2 (Single-Bounce Clustering): Next, we aim to cluster the point cloud $\mathcal{P}$ from (21) in order to associate the estimated single-bounce Doppler terms $\mathsf{f}_1(\mathbf{p})$ in (19) to specific objects in the environment. We perform clustering using DBSCAN[4] in the combined feature space comprising the 2D locations of points $\mathbf{p}$ and associated single-bounce Doppler terms $\mathsf{f}_1(\mathbf{p})$, similar to [66], [67], [68], [69], [70]. As suggested in [68], standard-score normalization is performed in each feature dimension to ensure independence to the physical units in any given dimension. The outputs of this stage are an estimate $\hat{\mathsf{M}}$ of the number of moving objects M in the environment and a mapping $\mathcal{C} : \mathcal{P} \to \{1, \ldots, \hat{\mathsf{M}}\}$ associating each point in the point cloud $\mathcal{P}$ to a specific cluster/object. For a cluster $m \in \{1, \ldots, \hat{\mathsf{M}}\}$, let $\mathbf{p}_m$ denote its 2D grid locations and $\mathbf{v}_m$ denote its unknown velocity vector. Post-clustering, the radar can associate the single-bounce Doppler terms estimated in Stage 1 to specific clusters, i.e., has estimates of $\mathsf{f}_1(\mathbf{v}_m;\mathbf{p}_m)$.

[4]DBSCAN is a common clustering algorithm used in the automotive radar literature, e.g., see [22], [66], [67], [68], [69], [70], which was first proposed in [71]. Robustness guarantees for DBSCAN are available in [72].

Stage 3 (Multi-Bounce Processing): The next stage involves estimating the multi-bounce Doppler terms for each point in the point cloud $\mathcal{P}$. Given N_1 clusters of static objects (via a similar clustering approach performed over the background data), let $\mathbf{p}_n$ denote grid locations belonging to clusters $n \in \{1, \ldots, \mathsf{N}_1\}$ and $\mathbf{p}_m$ denote grid locations belonging to moving object clusters $m \in \{1, \ldots, \hat{\mathsf{M}}\}$ as before. The radar performs multi-bounce Doppler processing via (17)–(18) for all possible pairs $(\mathbf{p}_m, \mathbf{p}_n)$ to estimate (a subset of) the corresponding double-bounce and triple-bounce Doppler terms $\mathsf{f}_2(\mathbf{v}_m; \mathbf{p}_m; \mathbf{p}_n)$, $\mathsf{f}_{3,\mathrm{I}}(\mathbf{v}_m; \mathbf{p}_m; \mathbf{p}_n)$, $\mathsf{f}_{3,\mathrm{II}}(\mathbf{v}_m; \mathbf{p}_m; \mathbf{p}_n)$.

Stage 4 (Full-Velocity Estimation): The radar then estimates the full-velocity vectors of *individual points* $\mathbf{p}_m$ belonging to a given moving object cluster $m \in \{1, \ldots, \hat{\mathsf{M}}\}$ by solving a least-squares problem similar to (15) by collecting Doppler measurements across all static object locations $\mathbf{p}_n$:

$$\mathbf{v}_{\mathbf{p}_m} = \arg\min_{\mathbf{w}} \left\| \begin{bmatrix} \mathsf{f}_1 \\ \mathsf{f}_2(\mathbf{p}_n) \\ \vdots \\ \mathsf{f}_{3,\mathrm{I}}(\mathbf{p}_n) \\ \vdots \\ \mathsf{f}_{3,\mathrm{II}}(\mathbf{p}_n) \\ \vdots \end{bmatrix} + \frac{1}{\lambda_{\mathsf{c}}} \begin{bmatrix} \frac{2\mathbf{p}_m^\top}{\|\mathbf{p}_m\|_2} \\ \frac{\mathbf{p}_m^\top}{\|\mathbf{p}_m\|_2} + \frac{(\mathbf{p}_m - \mathbf{p}_n)^\top}{\|\mathbf{p}_m - \mathbf{p}_n\|_2} \\ \vdots \\ \frac{2\mathbf{p}_m^\top}{\|\mathbf{p}_m\|_2} + \frac{2(\mathbf{p}_m - \mathbf{p}_n)^\top}{\|\mathbf{p}_m - \mathbf{p}_n\|_2} \\ \vdots \\ \frac{2(\mathbf{p}_m - \mathbf{p}_n)^\top}{\|\mathbf{p}_m - \mathbf{p}_n\|_2} \\ \vdots \end{bmatrix} \mathbf{w} \right\|_2^2,$$

where notational dependence on the cluster's unknown velocity vector $\mathbf{v}_m$ and locations $\mathbf{p}_m$ has been suppressed for clarity. The complexity of the above step can be reduced by pruning the set of static object locations to only correspond to those points $\mathbf{p}_n$ resulting in a specular reflection from the radar to the moving object location $\mathbf{p}_m$. We use this low complexity version of Stage 4 later in our evaluation in Section V.

Subsequently, within each cluster $m \in \{1, \ldots, \hat{\mathsf{M}}\}$, we perform clustering again via DBSCAN in the combined *location-velocity vector* feature space (with appropriate standard-score normalization) to find the appropriate set of locations $\mathbf{p}_m$ within the cluster whose velocity vectors are "close" to each other. Finally, the full-velocity vector $\mathbf{v}_m$ for the cluster is estimated as the average velocity vector of the points $\mathbf{p}_m$:

$$\mathbf{v}_m = \frac{1}{|\{\mathbf{p}_m\}|} \sum_{\{\mathbf{p}_m\}} \mathbf{v}_{\mathbf{p}_m}. \tag{22}$$

Computational Complexity: We break down the computational complexity calculation for our algorithm into four stages, and show that the overall complexity remains similar to state-of-the-art. Stages 1 & 2 correspond to single-bounce point cloud generation and clustering, which are standard steps performed by all automotive radars. Without any computational acceleration, single-bounce point cloud generation in Stage 1 has complexity $O(\mathsf{TRWP}_s)$, where T/R is the number of transmit/receive elements in the MIMO radar, W is the number of frequencies and P_s is the number of grid locations over which the single-bounce matched filtering is performed in (19) and (20). The computational complexity of DBSCAN in Stage 2 is $O(\mathsf{P}_s \log \mathsf{P}_s)$, see [71] for the calculation. The computational cost of Stage 3 is at most $O(\mathsf{TRWP}_s\mathsf{P}_m)$, where P_m is the number of moving object grid locations (see [48] for the calculation). The computational cost of solving the velocity vector estimation problem in Stage 4 across all moving object locations is $O(\mathsf{P}_s\mathsf{P}_m)$. Thus, the total computational complexity is simply $O(\mathsf{TRWP}_s\mathsf{P}_m)$. As mentioned above, the computational complexity is reduced in our evaluation by only considering those static object locations that result in a specular reflection from the radar to the moving object, making $\mathsf{P}_s \leq 6$ in our evaluation; making the overall cost linear in P_m. For state-of-the-art methods [18], [19], [20], [21], [22], [23], [24], [25] with N distributed radars, the overall computational complexity is $O(\mathsf{TRWNP}_m)$, which is also linear in P_m and remains similar to the complexity of our method.

IV. Theoretical Analysis

We present a series of theoretical results quantifying the impact of various system parameters on full-velocity estimation.

A. Conditions for Simplified Multi-Bounce Procedure in (18)

We begin by deriving conditions under which the multi-bounce Doppler estimation procedure in (17), which requires removing previously estimated terms from the measurements $\mathbf{y}(\omega; \ell)$, can be simplified into (18) that *does not* require removing any previously estimated terms. For simplicity, we derive the result for estimating double-bounce Doppler terms after estimating single-bounce Doppler terms, however the result holds even for estimating type-II triple-bounce after prior type-I triple-bounce estimation (or vice-versa).

Lemma 1: The simplification from (17) and (18) can be made when either of the following conditions hold:

$$\begin{aligned} &\left(\mathbf{a}_{\mathsf{RX}}(\theta_{\mathsf{r_m}}) \otimes \mathbf{a}_{\mathsf{TX}}(\theta_{\mathsf{r_m}})\right)^{\mathsf{H}} \left[\mathbf{a}_{\mathsf{RX}}(\theta_{\mathsf{r_m}}) \otimes \mathbf{a}_{\mathsf{TX}}(\theta_{\mathsf{r_s}}) \right. \\ &\quad \left. + \mathbf{a}_{\mathsf{RX}}(\theta_{\mathsf{r_s}}) \otimes \mathbf{a}_{\mathsf{TX}}(\theta_{\mathsf{r_m}})\right] = 0, \\ &\text{or, } \mathbf{a}_{\mathsf{TX}}^{\mathsf{H}}(\theta_{\mathsf{r_m}})\mathbf{a}_{\mathsf{TX}}(\theta_{\mathsf{r_s}}) = 0, \ \mathbf{a}_{\mathsf{RX}}^{\mathsf{H}}(\theta_{\mathsf{r_m}})\mathbf{a}_{\mathsf{RX}}(\theta_{\mathsf{r_s}}) = 0. \end{aligned}$$

Proof: See Supplementary Material.

In other words, (17) can be simplified into (18) as long as the transmit and receive array steering vectors along the single-bounce and double-bounce paths are orthogonal as per Lemma 1, i.e., the single-bounce and double-bounce paths can be resolved/separated in the angular domain by the radar. Moreover, it can be verified that the same conditions apply even to type-II triple-bounce Doppler estimation after estimating the type-I triple-bounce (or vice-versa) in around-corner scenarios [12] with no LOS paths to the moving objects. The conditions are rather mild and are further analyzed in the Supplementary Material.

B. Fundamental Limits of Double-Bounce Velocity Estimation

We begin by deriving fundamental limits for full-velocity estimation harnessing single-bounce and double-bounce scattering, neglecting higher-order multi-bounce for simplicity. We consider the toy example from Fig. 6 with two point objects - one static and the other moving. We first analyze the geometric

dilution-of-precision [11] for the least-squares problem in (15) solved as part of our overall pipeline. Subsequently, we analyze the end-to-end estimation error of our overall pipeline via a Cramér-Rao bound analysis.

1) Performance of (15): We start by quantifying the performance of (15) via the dilution-of-precision (DoP) [11].

*Definition 1 (*DoP *[11]):* Consider a linear system $\mathbf{y} = \mathbf{A}\mathbf{x} + \mathbf{n}$, with zero mean uncorrelated noise vector $\mathbf{n}$ with identity covariance. Let $\hat{\mathbf{x}}$ denote the pseudo-inverse solution for $\mathbf{x}$, i.e., $\hat{\mathbf{x}} = \mathbf{A}^{\dagger}\mathbf{y}$. The dilution-of-precision (DoP) quantifies the root-mean squared error (RMSE) for estimating $\mathbf{x}$,

$$\mathsf{DoP} = \sqrt{\mathbb{E}\left[\left\|\hat{\mathbf{x}} - \mathbf{x}\right\|_2^2\right]} = \sqrt{\mathsf{Tr}\left[\left(\mathbf{A}^{\top}\mathbf{A}\right)^{-1}\right]}.$$

Intuition: From its definition, it is clear that a smaller DoP implies a smaller estimation error, which is desirable. Well-conditioned matrices $\mathbf{A}$ have small DoP, e.g., $n \times n$ identity matrix has $\mathsf{DoP} = \sqrt{n}$. On the other hand, ill-conditioned, low rank matrices $\mathbf{A}$, e.g., an all-ones matrix, have infinitely large $\mathsf{DoP} \to \infty$. Hence, analyzing the DoP enables identifying regimes where the estimation error is expected to be small (at DoP minima) vs no estimation is possible (at DoP maxima).

In the context of our system, considering only single-bounce and double-bounce paths, the matrix $\mathbf{A}$ in Definition 1 corresponds to the upper 2×2 sub-matrix of (15):

$$\mathbf{A} = \begin{bmatrix} \frac{2\mathbf{r}_{\mathsf{m}}^{\top}}{\|\mathbf{r}_{\mathsf{m}}\|_2} \\ \frac{\mathbf{r}_{\mathsf{m}}^{\top}}{\|\mathbf{r}_{\mathsf{m}}\|_2} + \frac{(\mathbf{r}_{\mathsf{m}}-\mathbf{r}_{\mathsf{s}})^{\top}}{\|\mathbf{r}_{\mathsf{m}}-\mathbf{r}_{\mathsf{s}}\|_2} \end{bmatrix}. \tag{23}$$

In the following, we analyze the DoP for the simple configuration shown in Fig. 6, where the static object subtends an angle θ to the line joining the radar and the moving object.

Lemma 2: For the configuration shown in Fig. 6, the DoP as a function of angle $\theta \in [-180^{\circ}, 180^{\circ}]$ is given by

$$\mathsf{DoP} = \sqrt{\frac{3 - \cos(\theta)}{2\sin^2(\theta)}},$$

which peaks to infinity at $\theta \in \{0^{\circ}, \pm 180^{\circ}\}$, and has minimum value $(\frac{1}{2} + \frac{1}{\sqrt{2}}) \approx 1.2071$ at $\theta = \pm 2\tan^{-1}(2^{-\frac{1}{4}}) \approx \pm 80^{\circ}$.

Proof: See Supplementary Material.

Fig. 9 plots the DoP as a function of angle θ.

Intuition: Intuitively, one expects best performance when the objects are "perpendicular", i.e., $\theta \approx \pm 90^{\circ}$, in which case the single-bounce paths capture the radial velocity and the double-bounce paths capture the tangential velocity. While intuitive, the aforementioned statement is not strictly true because as per (23), both the single-bounce and double-bounce Doppler terms capture components of the radial velocity, in addition to the tangential velocity captured in double-bounce. Lemma 2 proves that $\theta \approx \pm 80^{\circ}$ is the optimal configuration.

We note however that the present DoP analysis is limited to only identifying optimal unit vector directions $\frac{\mathbf{r}_{\mathsf{m}}}{\|\mathbf{r}_{\mathsf{m}}\|_2}, \frac{\mathbf{r}_{\mathsf{m}}-\mathbf{r}_{\mathsf{s}}}{\|\mathbf{r}_{\mathsf{m}}-\mathbf{r}_{\mathsf{s}}\|_2}$, and not actual object locations $\mathbf{r}_{\mathsf{m}}, \mathbf{r}_{\mathsf{s}}$, due to the definition of the matrix $\mathbf{A}$ in (23). Moreover, the present result assumes perfect knowledge of the object locations, and hence matrix $\mathbf{A}$, for estimation. We overcome these drawbacks in the following Cramér-Rao bound analysis.

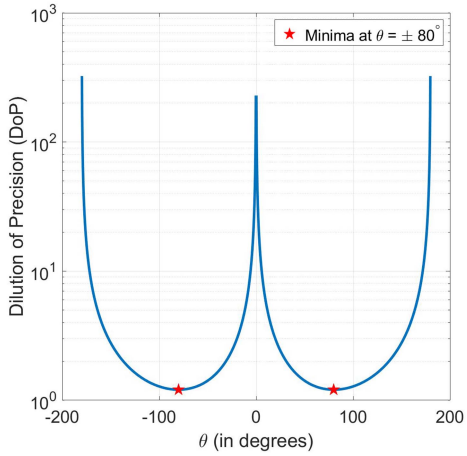

Fig. 9. Best performance when $\theta \approx \pm 80^{\circ}$ in Fig. 6.

2) Cramér-Rao Bound Analysis: Let $\mathbf{r}_{\mathsf{m}} = [x_{\mathsf{m}} \quad y_{\mathsf{m}}]^{\top}$ and $\mathbf{r}_{\mathsf{s}} = [x_{\mathsf{s}} \quad y_{\mathsf{s}}]^{\top}$ respectively denote the moving and static objects' 2D location vectors. Similarly, let $\mathbf{v}_{\mathsf{m}} = [v_{\mathsf{m}}^{x} \quad v_{\mathsf{m}}^{y}]^{\top}$ denote the moving object's 2D velocity vector. Furthermore, let $\sigma_{m/s}^{\mathsf{Re/Im}}$ denote the real/imaginary parts of the reflectivities of the moving and static objects. We derive Cramér-Rao bounds (CRB) for the vector of unknowns $\boldsymbol{\theta} = [\mathbf{r}_{\mathsf{m}}^{\top} \quad \mathbf{r}_{\mathsf{s}}^{\top} \quad \mathbf{v}_{\mathsf{m}}^{\top} \quad \sigma_{\mathsf{m}}^{\mathsf{Re}} \quad \sigma_{\mathsf{m}}^{\mathsf{Im}} \quad \sigma_{\mathsf{s}}^{\mathsf{Re}} \quad \sigma_{\mathsf{s}}^{\mathsf{Im}}]^{\top}$, where the reflectivites are considered nuisance parameters.

The radar's signal model is defined similar to (2):

$$\begin{aligned}\mathbf{y}(\omega;\ell) = \sqrt{\mathsf{P}_{\mathsf{TX}}}\Bigg[&\sigma_{\mathsf{m}}\left(\mathbf{a}_{\mathsf{RX}}(\theta_{\mathsf{m}}) \otimes \mathbf{a}_{\mathsf{TX}}(\theta_{\mathsf{m}})\right)\frac{e^{-j\left[\frac{\omega}{c}\mathsf{d}_{\mathsf{m}} + \frac{2\pi \mathsf{f}_{\mathsf{c}}}{c}\bar{\mathsf{v}}_{\mathsf{m}}\ell\mathsf{T}_{\mathsf{c}}\right]}}{4\pi^2\mathsf{d}_{\mathsf{m}}^2} \\ &+ \sigma_{\mathsf{m}}\sigma_{\mathsf{s}}\tilde{\mathbf{a}}_{\mathsf{m}}^{\mathsf{s}}\frac{e^{-j\left[\frac{\omega}{c}(\mathsf{d}_{\mathsf{m}}^{\mathsf{s}} + \frac{1}{2}\mathsf{d}_{\mathsf{m}} + \frac{1}{2}\mathsf{d}_{\mathsf{s}}) + \frac{2\pi \mathsf{f}_{\mathsf{c}}}{c}(\frac{1}{2}\bar{\mathsf{v}}_{\mathsf{m}} + \bar{\mathsf{v}}_{\mathsf{m}}^{\mathsf{s}})\ell\mathsf{T}_{\mathsf{c}}\right]}}{4\pi^2(\mathsf{d}_{\mathsf{m}}^{\mathsf{s}} + \frac{1}{2}\mathsf{d}_{\mathsf{m}} + \frac{1}{2}\mathsf{d}_{\mathsf{s}})^2} \\ &+ \sigma_{\mathsf{s}}\left(\mathbf{a}_{\mathsf{RX}}(\theta_{\mathsf{s}}) \otimes \mathbf{a}_{\mathsf{TX}}(\theta_{\mathsf{s}})\right)\frac{e^{-j\frac{\omega}{c}\mathsf{d}_{\mathsf{s}}}}{4\pi^2\mathsf{d}_{\mathsf{s}}^2}\Bigg] + \mathbf{n},\end{aligned} \tag{24}$$

where we have redefined (2) and restricted it up to double-bounce. Variable $\tilde{\mathbf{a}}_{\mathsf{m}}^{\mathsf{s}} = \mathbf{a}_{\mathsf{RX}}(\theta_{\mathsf{s}}) \otimes \mathbf{a}_{\mathsf{TX}}(\theta_{\mathsf{m}}) + \mathbf{a}_{\mathsf{RX}}(\theta_{\mathsf{m}}) \otimes \mathbf{a}_{\mathsf{TX}}(\theta_{\mathsf{s}})$ denotes the combined steering vector along double-bounce paths. Variables $\mathsf{d}_{\mathsf{m}} = 2\|\mathbf{r}_{\mathsf{m}}\|_2, \mathsf{d}_{\mathsf{s}} = 2\|\mathbf{r}_{\mathsf{s}}\|_2, \mathsf{d}_{\mathsf{m}}^{\mathsf{s}} = \|\mathbf{r}_{\mathsf{m}} - \mathbf{r}_{\mathsf{s}}\|_2$ denote the distances between the radar and moving object, radar and static object, and the static and moving objects respectively. Variables $\bar{\mathsf{v}}_{\mathsf{m}} = \frac{\mathbf{r}_{\mathsf{m}}^{\top}}{\|\mathbf{r}_{\mathsf{m}}\|_2}\mathbf{v}_{\mathsf{m}}$ and $\bar{\mathsf{v}}_{\mathsf{m}}^{\mathsf{s}} = \frac{(\mathbf{r}_{\mathsf{m}}-\mathbf{r}_{\mathsf{s}})^{\top}}{\|\mathbf{r}_{\mathsf{m}}-\mathbf{r}_{\mathsf{s}}\|_2}\mathbf{v}_{\mathsf{m}}$ denote the projection of the moving object's velocity vector $\mathbf{v}_{\mathsf{m}}$ onto the unit vectors along paths: radar $\to$ moving object and moving object $\to$ static object. We model the noise vector $\mathbf{n}$ to be complex Gaussian with identity covariance as in (2).

The CRB for the model in (24) is derived in Appendix A.

We now plot the derived CRB numerically for the configuration shown in Fig. 6, with unit-reflectivity objects at distances $\|\mathbf{r}_{\mathsf{m}}\|_2 = 2.5$ m and $\|\mathbf{r}_{\mathsf{m}} - \mathbf{r}_{\mathsf{s}}\|_2 = 2.5$ m, unless otherwise noted. We denote the angle subtended by static object onto the line joining the radar and the moving object by θ. The simulation

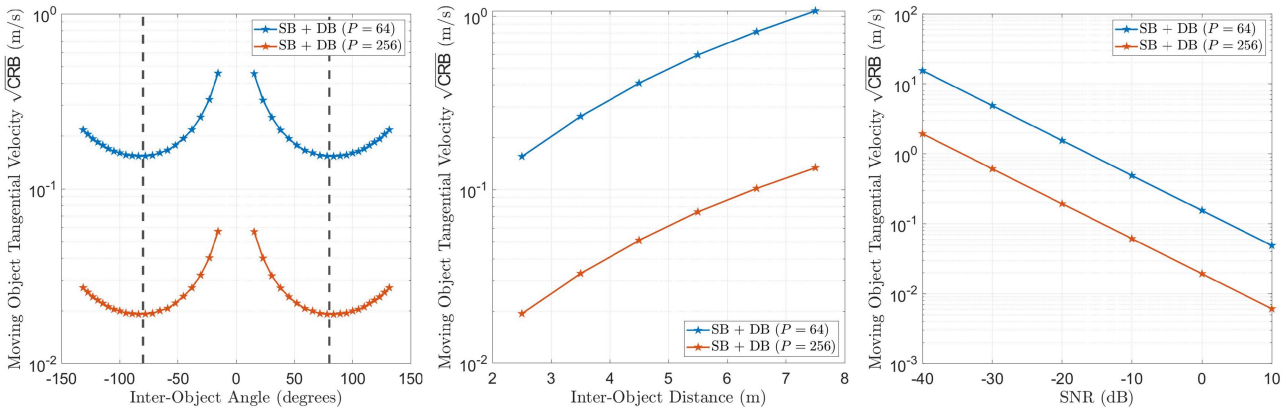

(a) $\sqrt{\mathsf{CRB}}$ vs θ. (b) $\sqrt{\mathsf{CRB}}$ vs $\|\mathbf{r}_\mathsf{m} - \mathbf{r}_\mathsf{s}\|_2$. (c) $\sqrt{\mathsf{CRB}}$ vs SNR.

Fig. 10. $\sqrt{\mathsf{CRB}}$ for moving object tangential velocity estimation vs angle θ, inter-object distance $\|\mathbf{r}_\mathsf{m} - \mathbf{r}_\mathsf{s}\|_2$ and signal-to-noise ratio (SNR) in Fig. 6. (a) Tangential velocity is best estimated when $\theta \approx \pm 80^\circ$, as also derived in Lemma 2 and shown in Fig. 9. (b) Tangential velocity is best estimated at small $\|\mathbf{r}_\mathsf{m} - \mathbf{r}_\mathsf{s}\|_2$ when the relative strength of double-bounce paths is large. (c) Inverse linear scaling with SNR, and more number of chirps L per frame improves tangential velocity estimation.

parameters correspond to a commercial off-the-shelf MIMO radar [7]: FMCW starting frequency $\mathsf{f}_\mathsf{c} = 77$ GHz, 4GHz bandwidth, $\mathsf{W} = 256$ instantaneous chirp frequencies, $\mathsf{L} = 64$ to 256 chirps per frame, chirp duration $\mathsf{T}_\mathsf{c} = 40\,\mu$s, and $\mathsf{T} = 9$, $\mathsf{R} = 16$ transmit/receive antennas.

Fig. 10 plots $\sqrt{\mathsf{CRB}}$, which lower bounds the root-mean squared error (RMSE) of any unbiased estimator, for estimating the moving object's tangential velocity[5] as a function of angle θ, distance $\|\mathbf{r}_\mathsf{m} - \mathbf{r}_\mathsf{s}\|_2$ and signal-to-noise ratio SNR $= \frac{1}{\mathsf{TRWL}} \sum_{\omega=1}^{\mathsf{W}} \sum_{\ell=1}^{\mathsf{L}} \|\mathbf{y}(\omega;\ell)\|_2^2$ (assuming identity covariance complex Gaussian noise $\mathbf{n}$ in (24)). Each plot is the average of 100 independent realizations of noise and $\mathbf{v}_\mathsf{m}$, with each entry uniformly distributed in $[-5, 5]$ m/s.

Fig. 10(a) corresponds to varying the angle θ, for SNR $= -20$ dB, showing that the tangential velocity is best estimated when $\theta \approx \pm 80^\circ$ and is worst estimated when $\theta \in \{0^\circ, \pm 180^\circ\}$, thus validating Lemma 2 and Fig. 9.

In the sequel, we consider $\theta = 90^\circ$, which is a near-optimal configuration as per Lemma 2 and Figs. 9 and 10(a), wherein the tangential velocity is along the line joining both objects.

Fig. 10(b) corresponds to varying distance $\|\mathbf{r}_\mathsf{m} - \mathbf{r}_\mathsf{s}\|_2$ from 2.5 m to 7.5 m by varying the static object's location $\mathbf{r}_2$, for SNR $= -20$ dB when $\|\mathbf{r}_\mathsf{m} - \mathbf{r}_\mathsf{s}\|_2 = 2.5$ m. Fig. 10(b) shows that larger values of $\|\mathbf{r}_\mathsf{m} - \mathbf{r}_\mathsf{s}\|_2$ result in poorer estimation of the static object's location $\mathbf{r}_\mathsf{s}$ and moving object's tangential velocity v_m^x, due to smaller double-bounce path strength.

Finally, Fig. 10(c) shows an inverse linear scaling of $\sqrt{\mathsf{CRB}}$ with the SNR. We also note that the curve for $\mathsf{L} = 256$ chirps per frame is lower than those for $\mathsf{L} = 64$ chirps per frame, indicating better estimation with more chirps per frame.

[5]More plots as a function of other system parameters - moving object location $\mathbf{r}_\mathsf{m}$, static object location $\mathbf{r}_\mathsf{s}$, and moving object velocity vector $\mathbf{v}_\mathsf{m}$ - are available in the Supplementary Material.

Further results quantifying the impact of multiple point-like static objects as well as extended static and moving objects are presented in the Supplementary Material.

C. Impact of Missing Terms in (15) & Utility of Triple-Bounce

Finally, we investigate the robustness of the least-squares problem in (15) to missing multi-bounce Doppler estimates.

Lemma 3: In the absence of noise, perfect estimation of $\mathbf{v}$ in (15) is possible from any combination of two or more Doppler terms amongst f_1, f_2, $\mathsf{f}_{3,\mathrm{I}}$, $\mathsf{f}_{3,\mathrm{II}}$, for all non-collinear static and moving object locations, $\mathbf{r}_\mathsf{s} \neq \alpha \mathbf{r}_\mathsf{m}$, $\forall \alpha \in \mathbb{R}$.

Proof: Recall the definitions of $\mathsf{f}_1, \mathsf{f}_2, \mathsf{f}_{3,\mathrm{I}}, \mathsf{f}_{3,\mathrm{II}}$ in (7)–(10). It is evident that the set of constitutent unit vectors, $\{\frac{\mathbf{r}_\mathsf{m}}{\|\mathbf{r}_\mathsf{m}\|_2}, \frac{\mathbf{r}_\mathsf{m}}{\|\mathbf{r}_\mathsf{m}\|_2} + \frac{\mathbf{r}_\mathsf{m} - \mathbf{r}_\mathsf{s}}{\|\mathbf{r}_\mathsf{m} - \mathbf{r}_\mathsf{s}\|_2}, \frac{\mathbf{r}_\mathsf{m} - \mathbf{r}_\mathsf{s}}{\|\mathbf{r}_\mathsf{m} - \mathbf{r}_\mathsf{s}\|_2}\}$ is linearly dependent; hence for any combination of ≥ 2 Doppler measurements amongst $\{\mathsf{f}_1, \mathsf{f}_2, \mathsf{f}_{3,\mathrm{I}}, \mathsf{f}_{3,\mathrm{II}}\}$, the rank of the matrix in (15) equals 2 (number of unknowns), provided $\frac{\mathbf{r}_\mathsf{m}}{\|\mathbf{r}_\mathsf{m}\|_2} \neq \frac{(\mathbf{r}_\mathsf{m} - \mathbf{r}_\mathsf{s})}{\|\mathbf{r}_\mathsf{m} - \mathbf{r}_\mathsf{s}\|_2}$, or equivalently, $\mathbf{r}_\mathsf{s} \neq \alpha \mathbf{r}_\mathsf{m}$, $\forall \alpha \in \mathbb{R}$.

Lemma 3 shows that triple-bounce paths due to the same pair of objects are not useful for full-velocity estimation in the presence of double-bounce. However, the above conclusion does not hold when either the static object is large enough to generate a diversity of double-bounce and triple-bounce paths passing through different points on the object surface, or in around-corner settings [12] with no direct LOS paths. In the latter scenario, velocity vector estimation of occluded moving objects can be performed via type-I and type-II triple-bounce.

V. Experimental Evaluation

We now experimentally demonstrate the benefits of using multi-bounce for full-velocity vector estimation using an open source experimental radar dataset from Mercedes-Benz [13]. The dataset comprises 21 different outdoor scenarios with 111 total recorded sequences, each collected over an average duration of 38.5 seconds. Each sequence consists of one moving

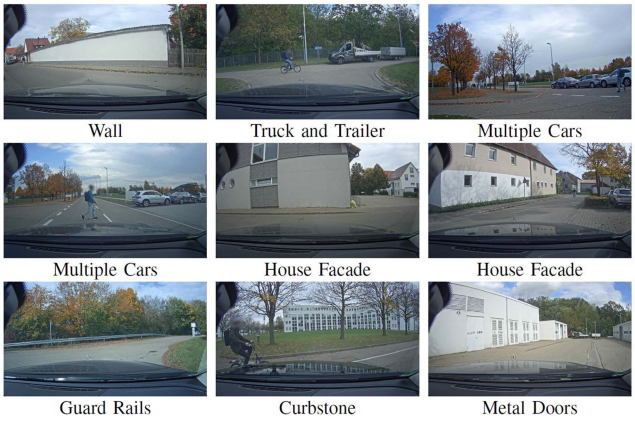

Fig. 11. Sample scenarios in dataset [13] ©2021 IEEE.

object - a pedestrian or a cyclist - that moves near one or more reflective surfaces. The reflective surfaces correspond to building walls, parked vehicles, road features (guard rails, curbstones), etc. Nine sample scenarios out of the 21 scenarios in the dataset are shown in Fig. 11. A stationary vehicle equipped with two 77 GHz MIMO radars records radar point clouds of the environment across the entire motion profile of the moving object. The technical specifications of the radars are as follows [13]: frame sampling frequency 10 Hz, maximum range 153 m, range resolution 0.15 m, azimuth field-of-view $\pm 70^\circ$, azimuth angular resolution 1.8°, maximum radial velocity ± 44.3 m/s, radial velocity resolution 0.087m/s.

A. Methodology

We adapt our proposed approach, outlined in Section III-B, to the dataset as follows.

Dataset Preprocessing: The dataset provides the locations and Doppler velocities for points in point clouds after preprocessing using CFAR detection and clustering, effectively equivalent to performing Stages 1-3 of our proposed algorithm from Section III-B. Each point in the point cloud is manually annotated as a background detection (for stationary objects, e.g., walls), a LOS moving object or a type-I or type-II multi-bounce "ghost" of the moving object (recall Figs. 4 and 5).

Procedure: Given Stages 1-3 have already been performed in the dataset, we adapt Stage 4 to the dataset as follows. Since millimeter-wave signals largely undergo specular scattering [73], instead of considering all background (static object) locations, we only consider background locations that would have resulted in a specular reflection towards a moving object at $\mathbf{p}_m$, which can be identified as the background location $\mathbf{p}_n$ that lies on the line joining the radar and a type-II double/triple-bounce "ghost" $\mathbf{p}_m^{\mathsf{DB/TB,II}}$ of the moving object $\mathbf{p}_m$, such that the following conditions are satisfied:

$$\ell_{\mathsf{DB}} = \|\mathbf{p}_n\|_2 + \|\mathbf{p}_n - \mathbf{p}_m\|_2 + \|\mathbf{p}_m\|_2 - 2\|\mathbf{p}_m^{\mathsf{DB,II}}\|_2 = 0, \quad (25)$$

$$\ell_{\mathsf{TB}} = 2\|\mathbf{p}_n\|_2 + 2\|\mathbf{p}_n - \mathbf{p}_m\|_2 - 2\|\mathbf{p}_m^{\mathsf{TB,II}}\|_2 = 0. \quad (26)$$

Letting $\mathcal{P}_{\mathsf{BG}}$ denote the background point cloud, the above procedure is equivalent to the following optimization problem:

$$\mathbf{p}_n = \arg\min_{\mathbf{p}\in\mathcal{P}_{\mathsf{BG}}} \left| \frac{y}{x} - \frac{y_m^{\mathsf{DB/TB,II}}}{x_m^{\mathsf{DB/TB,II}}} \right|^2 + |\ell_{\mathsf{DB/TB}}|^2 + \|\mathbf{p}\|_2 - \|\mathbf{p}_m^{\mathsf{DB/TB,II}}\|_2,$$

where $\mathbf{p} = [x \quad y]^\top$ and $\mathbf{p}_m^{\mathsf{DB/TB,II}} = [x_m^{\mathsf{DB/TB,II}} \quad y_m^{\mathsf{DB/TB,II}}]^\top$. The optimization problem is clearly non-convex, and hence is solved via exhaustive search. Subsequently, the remainder of the processing in Stage 4 is performed. Note that it suffices to consider type-II double/triple-bounce "ghosts" given the redundancy of type-I paths in the presence of type-II paths (recall Lemma 3 and Special Cases 1-3 from Section II-A). Moreover, determining appropriate background points for type-I "ghosts" requires determining their surface normals, which is beyond the scope of this work.

Baseline: As our baseline, we use single-radar methods [26], [27], [28] that estimate the full-velocity vectors of extended objects based on the single-bounce radial velocities measured for each point on the object. Mathematically, for an object composed of points $\mathbf{p}_k$, the velocity vector of the object is estimated by solving the following least-squares problem:

$$\mathbf{v} = \arg\min_{\mathbf{w}} \left\| \begin{bmatrix} \mathsf{f}_1(\mathbf{p}_1) \\ \vdots \\ \mathsf{f}_1(\mathbf{p}_k) \\ \vdots \end{bmatrix} + \frac{1}{\lambda_{\mathsf{c}}} \begin{bmatrix} \frac{2\mathbf{p}_1^\top}{\|\mathbf{p}_1\|_2} \\ \vdots \\ \frac{2\mathbf{p}_k^\top}{\|\mathbf{p}_k\|_2} \\ \vdots \end{bmatrix} \mathbf{w} \right\|_2^2,$$

which essentially corresponds to neglecting multi-bounce.

Performance Metrics: We quantify the performance of our approach using the velocity vector estimation error, i.e., the ℓ_2 norm between the estimated and ground truth velocity vectors. In certain results, we also quantify the error of the radial and tangential components of the velocity vector.

B. Results

We begin by demonstrating the gains provided by double-bounce over the single-bounce baseline [26], [27], [28]. Fig. 12(a) shows the cumulative distribution function (CDF) of the velocity vector estimation error across all 21 scenarios in the dataset; the 10th-90th percentile ranges for single-bounce and double-bounce velocity errors are [0.977,15.275] m/s and [0.341,3.472] m/s respectively. For comparison, the 10th-90th percentile range for the norm of the ground truth velocity vector is [2,4.143] m/s. The median error with double-bounce is 1.1 m/s, which is significantly smaller than the median velocity of 3.07 m/s and the median single-bounce error of 4.9 m/s. Overall, double-bounce improves the median velocity error by $4.5\times$ over the single-bounce baseline.

We further show in the Supplementary Material that the major contributor to the gains with double-bounce is the significantly better tangential velocity estimation; the radial velocity estimation performance of both the proposed method and the single-bounce baseline remains similar. Additional results with

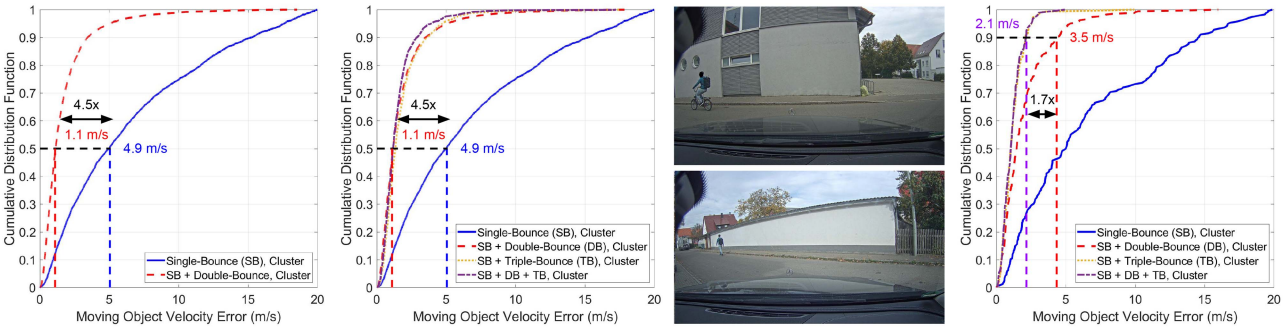

(a) Velocity vector error CDF. (b) Triple-bounce error CDF. (c) Large walls [13]. (d) Triple-bounce CDF for (c).

Fig. 12. Double-bounce and triple-bounce single-reflector velocity vector estimation results. (a) Proposed approach results in $4.5\times$ improvement in median estimation error over single-bounce baseline. (b)–(d) Triple-bounce does not improve velocity error CDF across all 21 scenarios, except in scenarios with large reflecting walls, e.g., those shown in (c) [13] ©2021 IEEE.

different reflector materials and multiple reflectors are also presented in the Supplementary Material.

Finally, we quantify the gains possible with triple-bounce. Fig. 12(b) shows the CDF across all 21 scenarios remains unchanged on incorporating triple-bounce, consistent with the findings of Lemma 3. However, in certain scenarios like those shown in Fig. 12(c) with large reflecting walls, there is clear benefit of triple-bounce, reducing the 90th percentile velocity error from 3.472 m/s to 2.141 m/s in Fig. 12(d). In such cases, the point object assumption used to derive Lemma 3 no longer holds; making it possible that the double-bounce and triple-bounce paths correspond to reflections from different points on the wall surface. This diversity of reflecting points on the wall surface explains the gains with triple-bounce.

In the Supplementary Material, we present additional results quantifying the performance with more than 1 moving object.

VI. Concluding Remarks

In this paper, we presented a method enabling standalone MIMO radars to estimate the full-velocity vectors of moving objects within a single radar frame by exploiting multi-bounce scattering from secondary static objects in the environment, e.g., building pillars, walls, etc. Via extensive theoretical and experimental evaluation, we demonstrated a $4.5\times$ reduction in the velocity vector estimation error over comparable baselines.

There are multiple avenues for future work. One direction would be to integrate the proposed method with existing solutions based on multi-frame object tracking [14], [15], [16] and multiple radar and/or camera modules [6], [18], [19], [20], [21], [22], [23], [24], [25]. Furthermore, we assumed a static radar in this work; incorporating the method with ego-motion algorithms [74], [75], [76] would be key for incorporating our method into automotive navigation systems. Our present evaluation was also limited to 2D due to the limited availability of 3D radar datasets and lack of high-resolution elevation processing in commercial MIMO radar testbeds. The performance of our algorithm also heavily depends on the accuracy of clustering; future work will evaluate the performance impact of clustering errors and the clutter due to > 2 moving objects in the environment. Future work will also evaluate the benefits of our method for 3D velocity vector estimation, which would be of great utility in autonomous aerial mobility scenarios. Finally, this work leveraged multi-bounce scattering from ambient static objects in the environment. Two interesting avenues for future work would be: (i) to design and deploy dedicated reflectors in the environment, similar to [77], [78], [79], that provide strong multi-bounce components - enabling vehicle-mounted radars to estimate the full-velocity vectors of moving objects, and (ii) exploiting multi-bounce between multiple moving objects, e.g., moving vehicles on highways.

Appendix A
Cramér-Rao Bound Derivation (Section IV-B2)

We derive the CRB based on the following standard results.

Theorem 1 (Vector CRB [80]): The covariance matrix of any unbiased estimator $\hat{\boldsymbol{\theta}}$ of a real parameter vector $\boldsymbol{\theta}$ satisfies:

$$\mathrm{cov}(\hat{\boldsymbol{\theta}}) = \mathbb{E}\left[\left(\hat{\boldsymbol{\theta}} - \boldsymbol{\theta}\right)\left(\hat{\boldsymbol{\theta}} - \boldsymbol{\theta}\right)^{\top}\right] \succeq \mathbf{J}^{-1}(\boldsymbol{\theta}),$$

where $\mathbf{J}(\boldsymbol{\theta})$ is the Fischer information matrix (FIM):

$$\mathbf{J}(\boldsymbol{\theta}) = -\mathbb{E}\left[\frac{\partial}{\partial \boldsymbol{\theta}}\left[\frac{\partial \ln p(\mathbf{y};\boldsymbol{\theta})}{\partial \boldsymbol{\theta}}\right]^{\top}\right],$$

and $p(\mathbf{y};\boldsymbol{\theta})$ denotes the likelihood of measurements $\mathbf{y}$, which satisfies the regularity condition $\mathbb{E}\left[\frac{\partial \ln p(\mathbf{y};\boldsymbol{\theta})}{\partial \boldsymbol{\theta}}\right] = \mathbf{0}$, $\forall \boldsymbol{\theta}$.

Lemma 4 (FIM for Transformed Parameters [80]): The Fischer information matrix (FIM) $\mathbf{J}(\boldsymbol{\theta})$ for a parameter vector $\boldsymbol{\theta}$ can be expressed in terms of the FIM $\mathbf{J}(\boldsymbol{\varphi})$ for a transformed parameter vector $\boldsymbol{\varphi}$ as $\mathbf{J}(\boldsymbol{\theta}) = \mathbf{P}\mathbf{J}(\boldsymbol{\varphi})\mathbf{P}^{\top}$, where $\mathbf{P} = \frac{\partial \boldsymbol{\varphi}^{\top}}{\partial \boldsymbol{\theta}}$.

Lemma 5 (FIM for Complex Gaussian Likelihood [81]): For measurements following a complex Gaussian likelihood, $p(\mathbf{y};\boldsymbol{\theta}) = \mathcal{CN}(\boldsymbol{\mu}_{\boldsymbol{\theta}}, \boldsymbol{\Sigma})$, the FIM $\mathbf{J}(\boldsymbol{\theta})$ can be expressed as:

$$\mathbf{J}(\boldsymbol{\theta}) = \left(\frac{\partial \boldsymbol{\mu}_{\boldsymbol{\theta}}^{*}}{\partial \boldsymbol{\theta}^{*}}\right)\boldsymbol{\Sigma}^{-1}\left(\frac{\partial \boldsymbol{\mu}_{\boldsymbol{\theta}}}{\partial \boldsymbol{\theta}}\right)^{\top} + \left(\frac{\partial \boldsymbol{\mu}_{\boldsymbol{\theta}}}{\partial \boldsymbol{\theta}^{*}}\right)(\boldsymbol{\Sigma}^{-1})^{*}\left(\frac{\partial \boldsymbol{\mu}_{\boldsymbol{\theta}}^{*}}{\partial \boldsymbol{\theta}}\right)^{\top}.$$

The specific CRB expressions for our signal model in (24) can be found in the Supplementary Material.

REFERENCES

[1] N. Mehrotra, D. Pandey, U. Madhow, Y. Mostofi, and A. Sabharwal, "Instantaneous velocity vector estimation using a single MIMO radar via multi-bounce scattering," in *Proc. IEEE Conf. Comput. Imag. Using Synthetic Apertures*, 2024, pp. 1–5.

[2] S. Sun, A. P. Petropulu, and H. V. Poor, "MIMO radar for advanced driver-assistance systems and autonomous driving: Advantages and challenges," *IEEE Signal Process. Mag.*, vol. 37, no. 4, pp. 98–117, Jul. 2020.

[3] Y. Li and J. Ibanez-Guzman, "Lidar for autonomous driving: The principles, challenges, and trends for automotive lidar and perception systems," *IEEE Signal Process. Mag.*, vol. 37, no. 4, pp. 50–61, Jul. 2020.

[4] M. Markel, *Radar for Fully Autonomous Driving*. Norwood, MA, USA: Artech House, 2022.

[5] S. Sun and Y. D. Zhang, "4D automotive radar sensing for autonomous vehicles: A sparsity-oriented approach," *IEEE J. Sel. Topics Signal Process.*, vol. 15, no. 4, pp. 879–891, Jun. 2021.

[6] Y. Long, D. Morris, X. Liu, M. Castro, P. Chakravarty, and P. Narayanan, "Full-velocity radar returns by radar-camera fusion," in *Proc. IEEE/CVF Int. Conf. Comput. Vis.*, Oct. 2021, pp. 16178–16187.

[7] T. Instruments, "AWR2243 four-chip cascade mmWave radar," 2019. [Online]. Available: https://www.ti.com/tool/TIDEP-01012

[8] T. Instruments, "TI radar academy," 2024. [Online]. Available: https://dev.ti.com/tirex/explore/node?node=A__AUAJwr4zBXhyz-M3VG2cUg__RADAR-ACADEMY__GwxShWe__LATEST

[9] N. Mehrotra and A. Sabharwal, "When does multipath improve imaging resolution?," *IEEE J. Sel. Areas Inf. Theory*, vol. 3, no. 1, pp. 135–146, Mar. 2022.

[10] M. R. Akdeniz et al., "Millimeter wave channel modeling and cellular capacity evaluation," *IEEE J. Sel. Areas Commun.*, vol. 32, no. 6, pp. 1164–1179, Jun. 2014.

[11] R. B. Langley et al., "Dilution of precision," *GPS World*, vol. 10, no. 5, pp. 52–59, 1999.

[12] N. Scheiner et al., "Seeing around street corners: Non-line-of-sight detection and tracking in-the-wild using doppler radar," in *Proc. IEEE/CVF Conf. Comput. Vis. Pattern Recognit.*, Jun. 2020, pp. 2065–2074.

[13] F. Kraus, N. Scheiner, W. Ritter, and K. Dietmayer, "The radar ghost dataset–an evaluation of ghost objects in automotive radar data," in *Proc. 2021 IEEE/RSJ Int. Conf. Intell. Robots Syst.*, 2021, pp. 8570–8577.

[14] J. Gunnarsson, L. Svensson, L. Danielsson, and F. Bengtsson, "Tracking vehicles using radar detections," in *Proc. IEEE Intell. Veh. Symp.*, 2007, pp. 296–302.

[15] C. Knill, A. Scheel, and K. Dietmayer, "A direct scattering model for tracking vehicles with high-resolution radars," in *Proc. IEEE Intell. Veh. Symp.*, 2016, pp. 298–303.

[16] N. B. Gosala and X. Meng, "An RLS-based instantaneous velocity estimator for extended radar tracking," in *Proc. IEEE/RSJ Int. Conf. Intell. Robots Syst.*, 2020, pp. 2273–2280.

[17] A. Devices, "From ADAS to driver replacement—Is actual radar performance good enough?" 2024. [Online]. Available: https://www.analog.com/en/signals/thought-leadership/from-adas-to-driver-replacement.html

[18] E. Insanic and P. R. Siqueira, "A maximum likelihood approach to estimation of vector velocity in Doppler radar networks," *IEEE Trans. Geosci. Remote Sens.*, vol. 50, no. 2, pp. 553–567, Feb. 2012.

[19] D. Kellner, M. Barjenbruch, J. Klappstein, J. Dickmann, and K. Dietmayer, "Instantaneous full-motion estimation of arbitrary objects using dual Doppler radar," in *Proc. IEEE Intell. Veh. Symp. Proc.*, 2014, pp. 324–329.

[20] S. Edstaller and D. Mueller, "A cooperative radar system with active reference target synchronization for kinematic target analysis," *IEEE Trans. Microw. Theory Techn.*, vol. 69, no. 9, pp. 4118–4131, Sep. 2021.

[21] S.-G. Lee, J. Jung, and S.-C. Kim, "Enhanced velocity vector estimation using distributed radar system," in *Proc. IEEE VTS Asia Pacific Wireless Commun. Symp.*, 2022, pp. 75–79.

[22] J. Schlichenmaier, M. Steiner, T. Grebner, and C. Waldschmidt, "Clustering and subsequent contour and motion estimation of automotive objects using a network of cooperative radar sensors," *IEEE Trans. Veh. Technol.*, vol. 72, no. 1, pp. 428–443, Jan. 2023.

[23] Y. Zhao, L. Wimmer, V. Sark, M. Krstic, and E. Grass, "Instantaneous 3D velocity estimation using coordinated OFDM radar nodes," in *Proc. 24th Int. Radar Symp.*, 2023, pp. 1–10.

[24] B. Meinecke, D. Werbunat, P. Schoeder, and C. Waldschmidt, "Matching bistatic target responses in radar networks to enable vectorial velocity estimation," in *Proc. 18th Eur. Radar Conf.*, 2022, pp. 42–45.

[25] B. Meinecke, M. Steiner, J. Schlichenmaier, and C. Waldschmidt, "Instantaneous target velocity estimation using a network of a radar and repeater elements," in *Proc. 16th Eur. Radar Conf.*, 2019, pp. 241–244.

[26] D. Kellner, M. Barjenbruch, K. Dietmayer, J. Klappstein, and J. Dickmann, "Instantaneous lateral velocity estimation of a vehicle using Doppler radar," in *Proc. 16th Int. Conf. Inf. Fusion*, 2013, pp. 877–884.

[27] J. Schlichenmaier, L. Yan, M. Stolz, and C. Waldschmidt, "Instantaneous actual motion estimation with a single high-resolution radar sensor," in *Proc. IEEE MTT-S Int. Conf. Microw. Intell. Mobility*, 2018, pp. 1–4.

[28] N. Singh, D. Sil, and A. Sharma, "Parallelized instantaneous velocity and heading estimation of objects using single imaging radar," in *Proc. IEEE Radar Conf.*, 2021, pp. 1–6.

[29] M. Leigsnering, M. Amin, F. Ahmad, and A. M. Zoubir, "Multipath exploitation and suppression for SAR imaging of building interiors: An overview of recent advances," *IEEE Signal Process. Mag.*, vol. 31, no. 4, pp. 110–119, Jul. 2014.

[30] G. Gennarelli and F. Soldovieri, "Multipath ghosts in radar imaging: Physical insight and mitigation strategies," *IEEE J. Sel. Topics Appl. Earth Observ. Remote Sens.*, vol. 8, no. 3, pp. 1078–1086, Mar. 2015.

[31] R. Feng, E. D. Greef, M. Rykunov, H. Sahli, S. Pollin, and A. Bourdoux, "Multipath ghost recognition for indoor MIMO radar," *IEEE Trans. Geosci. Remote Sens.*, vol. 60, 2022, Art. no. 5104610.

[32] L. Zheng, J. Long, M. Lops, F. Liu, X. Hu, and C. Zhao, "Detection of ghost targets for automotive radar in the presence of multipath," *IEEE Trans. Signal Process.*, vol. 72, pp. 2204–2220, 2024, doi: 10.1109/TSP.2024.3384750.

[33] W. Chen et al., "Environment-aware multi-person tracking in indoor environments with mmWave radars," *Proc. ACM Interactive, Mobile, Wearable Ubiquitous Technol.*, vol. 7, no. 3, pp. 1–29, Sep. 2023, doi: 10.1145/3610902.

[34] O. Biallawons and J. H. G. Ender, "Multipath detection by using space-space adaptive processing (SSAP) with MIMO radar," in *Proc. 2018 Int. Conf. Radar*, 2018, pp. 1–4.

[35] S. Yue, H. He, P. Cao, K. Zha, M. Koizumi, and D. Katabi, "CornerRadar: RF-Based indoor localization around corners," *Proc. ACM Interactive Mobile Wearable Ubiquitous Technol.*, vol. 6, no. 1, pp. 1–24, Mar. 2022, doi: 10.1145/3517226.

[36] T. Woodford, X. Zhang, E. Chai, and K. Sundaresan, "Mosaic: Leveraging diverse reflector geometries for omnidirectional around-corner automotive radar," in *Proc. 20th Annu. Int. Conf. Mobile Syst., Appl. Serv., (MobiSys'22)*, New York, NY, USA, 2022, pp. 155–167, doi: 10.1145/3498361.3538944.

[37] S. K. Doddalla and G. C. Trichopoulos, "Non-line of sight terahertz imaging from a single viewpoint," in *Proc. IEEE/MTT-S Int. Microw. Symp.*, 2018, pp. 1527–1529.

[38] M. Aladsani, A. Alkhateeb, and G. C. Trichopoulos, "Leveraging mmWave imaging and communications for simultaneous localization and mapping," in *Proc. IEEE Int. Conf. Acoust., Speech Signal Process.*, 2019, pp. 4539–4543.

[39] Y. Cui and G. C. Trichopoulos, "Seeing around obstacles using active terahertz imaging," *IEEE Trans. Terahertz Sci. Technol.*, vol. 14, no. 4, pp. 433–445, 2024, doi: 10.1109/TTHZ.2024.3401041.

[40] X. Liu, S. Wei, J. Wei, J. Shi, X. Zhang, and Y. Li, "Non-line-of-sight millimeter-wave radar 3-D sparse reconstruct via MSSTV method," in *Proc. IEEE 9th Int. Symp. Microw., Antenna, Propag. EMC Technol. Wireless Commun.*, 2022, pp. 424–427.

[41] J. Chen et al., "Joint estimation of NLOS building layout and targets via sparsity-driven approach," *IEEE Trans. Geosci. Remote Sens.*, vol. 60, 2022, Art. no. 5114513.

[42] Q. Tang, J. Li, L. Wang, Y. Jia, and G. Cui, "Multipath imaging for NLOS targets behind an L-shaped corner with single-channel UWB radar," *IEEE Sensors J.*, vol. 22, no. 2, pp. 1531–1540, Jan. 2022.

[43] S. Wei et al., "Nonline-of-sight 3-D imaging using millimeter-wave radar," *IEEE Trans. Geosci. Remote Sens.*, vol. 60, 2022, Art. no. 5106518.

[44] M. Levy-Israel, I. Bilik, and J. Tabrikian, "MCRB on DOA estimation for automotive MIMO radar in the presence of multipath," *IEEE Trans. Aerosp. Electron. Syst.*, vol. 59, no. 5, pp. 4831–4843, Oct. 2023.

[45] P. Setlur and N. Devroye, "Multipath exploited Bayesian and Cramer-Rao bounds for single-sensor target localization," *EURASIP J. Adv. Signal Process.*, vol. 2013, pp. 1–23, 2013.

[46] Z. Hao, H. Yan, X. Dang, Z. Ma, P. Jin, and W. Ke, "Millimeter-wave radar localization using indoor multipath effect," *Sensors*, vol. 22, no. 15, 2022, Art. no. 5671. [Online]. Available: https://www.mdpi.com/1424-8220/22/15/5671

[47] Z. Li, Z. Tian, Z. Wang, and Z. Zhang, "Multipath-assisted indoor localization using a single receiver," *IEEE Sensors J.*, vol. 21, no. 1, pp. 692–705, Jan. 2021.
[48] N. Mehrotra, D. Pandey, A. Prabhakara, Y. Liu, S. Kumar, and A. Sabharwal, "Hydra: Exploiting multi-bounce scattering for beyond-field-of-view mmWave radar," in *Proc. 30th Annu. Int. Conf. Mobile Comput. Netw.*, in ACM MobiCom'24, New York, NY, USA, 2024, pp. 1545–1559, doi: 10.1145/3636534.3690710.
[49] M. Cheney and R. J. Bonneau, "Imaging that exploits multipath scattering from point scatterers," *Inverse Problems*, vol. 20, no. 5, 2004, Art. no. 1691.
[50] S. Kidera, T. Sakamoto, and T. Sato, "Extended imaging algorithm based on aperture synthesis with double-scattered waves for UWB radars," *IEEE Trans. Geosci. Remote Sens.*, vol. 49, no. 12, pp. 5128–5139, Dec. 2011.
[51] O. Biallawons and J. H. G. Ender, "Virtual multistatic illumination by exploitation of multipath propagation with coherent MIMO radar," in *Proc. IEEE Radar Conf.*, 2020, pp. 1–5.
[52] L. Li and J. L. Krolik, "Simultaneous target and multipath positioning," *IEEE J. Sel. Topics Signal Process.*, vol. 8, no. 1, pp. 153–165, Feb. 2014.
[53] R. Feng, E. D. Greef, M. Rykunov, S. Pollin, A. Bourdoux, and H. Sahli, "Multipath ghost recognition and joint target tracking with wall estimation for indoor MIMO radar," *IEEE Trans. Radar Syst.*, vol. 2, pp. 154–164, 2024.
[54] F. Zhang, J. Xiong, Z. Chang, J. Ma, and D. Zhang, "Mobi2Sense: Empowering wireless sensing with mobility," in *Proc. 28th Annu. Int. Conf. Mobile Comput. Netw., (MobiCom'22)*, New York, NY, USA, 2022, pp. 268–281, doi: 10.1145/3495243.3560518.
[55] R. G. Guendel, N. C. Kruse, F. Fioranelli, and A. Yarovoy, "Multipath exploitation for human activity recognition using a radar network," *IEEE Trans. Geosci. Remote Sens.*, vol. 62, 2024, Art. no. 5103013.
[56] A. Battaglia, S. Tanelli, S. Kobayashi, D. Zrnic, R. J. Hogan, and C. Simmer, "Multiple-scattering in radar systems: A review," *J. Quantitative Spectrosc. Radiative Transfer*, vol. 111, no. 6, pp. 917–947, 2010. [Online]. Available: https://www.sciencedirect.com/science/article/pii/S0022407309003677
[57] K. T. Selvan and R. Janaswamy, "Fraunhofer and Fresnel distances: Unified derivation for aperture antennas," *IEEE Antennas Propag. Mag.*, vol. 59, no. 4, pp. 12–15, Aug. 2017.
[58] M. F. Keskin, H. Wymeersch, and V. Koivunen, "Monostatic sensing with OFDM under phase noise: From mitigation to exploitation," *IEEE Trans. Signal Process.*, vol. 71, pp. 1363–1378, 2023.
[59] D. Bilibashi, E. M. Vitucci, and V. Degli-Esposti, "Dynamic ray tracing: Introduction and concept," in *Proc. 14th Eur. Conf. Antennas Propag.*, 2020, pp. 1–5.
[60] NVIDIA, "Sionna v0.17 ray tracing documentation," 2024. [Online]. Available: https://nvlabs.github.io/sionna/api/rt.html#sionna.rt.Paths.apply_doppler
[61] T. S. Rappaport, E. Ben-Dor, J. N. Murdock, and Y. Qiao, "38 GHz and 60 GHz angle-dependent propagation for cellular & peer-to-peer wireless communications," in *Proc. IEEE Int. Conf. Commun.*, 2012, pp. 4568–4573.
[62] D. Tse and P. Viswanath, *Fundamentals of Wireless Communication*. New York, NY, USA: Cambridge Univ. Press, 2005.
[63] K. Kulpa, "The CLEAN type algorithms for radar signal processing," in *Proc. 2008 Microw., Radar Remote Sens. Symp.*, 2008, pp. 152–157.
[64] J. Li and P. Stoica, *MIMO Radar Signal Processing*. Hoboken, NJ, USA: Wiley, 2008.
[65] H. Rohling, "Ordered statistic CFAR technique - An overview," in *Proc. 12th Int. Radar Symp.*, 2011, pp. 631–638.
[66] E. Schubert, F. Meinl, M. Kunert, and W. Menzel, "Clustering of high resolution automotive radar detections and subsequent feature extraction for classification of road users," in *Proc. 16th Int. Radar Symp.*, 2015, pp. 174–179.
[67] J. Schlichenmaier, F. Roos, P. Hügler, and C. Waldschmidt, "Clustering of closely adjacent extended objects in radar images using velocity profile analysis," in *Proc. 2019 IEEE MTT-S Int. Conf. Microw. Intell. Mobility*, 2019, pp. 1–4.
[68] Q. Wen and S. Cao, "Radar range–Doppler flow: A radar signal processing technique to enhance radar target classification," *IEEE Trans. Aerosp. Electron. Syst.*, vol. 60, no. 2, pp. 1519–1529, Apr. 2024.
[69] N. Scheiner, N. Appenrodt, J. Dickmann, and B. Sick, "A multi-stage clustering framework for automotive radar data," in *Proc. IEEE Intell. Transp. Syst. Conf.*, 2019, pp. 2060–2067.
[70] Z. Ren, J. Tabrikian, I. Bilik, and W. Yi, "Discrimination of automotive radar distributed targets," in *Proc. IEEE Int. Radar Conf.*, 2023, pp. 1–6.
[71] M. Ester, H.-P. Kriegel, J. Sander, and X. Xu, "A density-based algorithm for discovering clusters in large spatial databases with noise," in *Proc. KDD*, 1996, vol. 96, no. 34, pp. 226–231.
[72] H. Jiang, J. Jang, and O. Nachum, "Robustness guarantees for density clustering," in *Proc. 22nd Int. Conf. Artif. Intell. Statist.*, in Proceedings of Machine Learning Research, K. Chaudhuri and M. Sugiyama, Eds., 2019, vol. 89, pp. 3342–3351. [Online]. Available: https://proceedings.mlr.press/v89/jiang19a.html
[73] T. S. Rappaport, G. R. MacCartney, M. K. Samimi, and S. Sun, "Wideband millimeter-wave propagation measurements and channel models for future wireless communication system design," *IEEE Trans. Commun.*, vol. 63, no. 9, pp. 3029–3056, Sep. 2015.
[74] D. Kellner, M. Barjenbruch, J. Klappstein, J. Dickmann, and K. Dietmayer, "Instantaneous ego-motion estimation using doppler radar," in *Proc. 16th Int. IEEE Conf. Intell. Transp. Syst.*, 2013, pp. 869–874.
[75] M. Hoffmann, L. Krabbe, C. Schüßler, P. Gulden, and M. Vossiek, "Instantaneous ego-motion estimation using a coherent radar network," in *Proc. 19th Eur. Radar Conf.*, 2022, pp. 321–324.
[76] A. Galeote-Luque, V. Kubelka, M. Magnusson, J.-R. Ruiz-Sarmiento, and J. Gonzalez-Jimenez, "Doppler-only single-scan 3D vehicle odometry," in *Proc. 2024 IEEE Int. Conf. Robot. Autom. (ICRA)*, 2024, pp. 13703–13709, doi: 10.1109/ICRA57147.2024.10611199.
[77] A. Aubry, A. D. Maio, and M. Rosamilia, "Reconfigurable intelligent surfaces for N-LOS radar surveillance," *IEEE Trans. Veh. Technol.*, vol. 70, no. 10, pp. 10735–10749, Oct. 2021.
[78] K. Meng, Q. Wu, R. Schober, and W. Chen, "Intelligent reflecting surface enabled multi-target sensing," *IEEE Trans. Commun.*, vol. 70, no. 12, pp. 8313–8330, Dec. 2022.
[79] D. Xie, X. Wang, and A. Tang, "MetaSight: Localizing blocked RFID objects by modulating NLOS signals via metasurfaces," in *Proc. 20th Annu. Int. Conf. Mobile Syst., Appl. Serv., (MobiSys'22)*, New York, NY, USA, 2022, pp. 504–516, doi: 10.1145/3498361.3538947.
[80] S. M. Kay, *Fundamentals of Statistical Signal Processing: Estimation Theory*. Upper Saddle River, NJ, USA: Prentice-Hall, 1993.
[81] C. D. Richmond and L. L. Horowitz, "Parameter bounds on estimation accuracy under model misspecification," *IEEE Trans. Signal Process.*, vol. 63, no. 9, pp. 2263–2278, May 2015.

Nishant Mehrotra received the B.Tech. degree (with Hons.) in electronics and electrical communication engineering from the Indian Institute of Technology, Kharagpur, Kharagpur, India, in 2018, and the M.S. and Ph.D. degrees in electrical and computer engineering from Rice University, Houston, TX, USA, in 2020 and 2024, respectively. He is currently a Postdoctoral Associate with Duke University, Durham, NC, USA. His research interests include radar sensing, next-generation wireless systems, joint sensing-communication, and information theory.

Divyanshu Pandey received the B.Tech. degree in communication and computer engineering from the LNM Institute of Information Technology, Jaipur, India, in 2011, the M.S. degree in electrical engineering from the University of Minnesota, Twin Cities, MN, USA, in 2014, and the Ph.D. degree in electrical engineering from McGill University, Montreal, QC, Canada, in 2022. From 2011 to 2013, he was an Instrumentation Engineer with HMEL, Bathinda, India. He was a Wireless Systems Engineer with Marvell Semiconductor, Santa Clara, CA, USA, from 2015 to 2017, and a Postdoctoral Associate with the Department of Electrical and Computer Engineering, Rice University, Houston, TX, USA, from 2023 to 2025. He is currently a Wireless Systems Engineer with Apple, Santa Clara Valley, CA, USA. His research interests include wireless communication systems, information theory, joint sensing and communication systems, and tensor algebra with applications to communications and signal processing.

Upamanyu Madhow (Fellow, IEEE) received the bachelor's degree in electrical engineering from the Indian Institute of Technology Kanpur, Kanpur, India, in 1985, and the Ph.D. degree in electrical engineering from the University of Illinois, Urbana-Champaign, Champaign, IL, USA, in 1990. He was a Research Scientist with Bell Communications Research, Morristown, NJ, USA, and a faculty member with the University of Illinois, Urbana-Champaign. He is currently a Professor of electrical and computer engineering (ECE) with the University of California, Santa Barbara, Santa Barbara, CA, USA. He is the author of two textbooks published by Cambridge University Press, Fundamentals of Digital Communication in 2008, and Introduction to Communication Systems in 2014. His current research interests include next generation infrastructures for robust and energy-efficient communication, sensing, learning and inference. Dr. Madhow is a recipient of the 1996 NSF CAREER award, co-recipient of the 2012 IEEE Marconi prize paper award in wireless communications, and 2018 Distinguished Alumni award from the ECE Department, UIUC. He was an Associate Editor for IEEE TRANSACTIONS ON COMMUNICATIONS, IEEE TRANSACTIONS ON INFORMATION THEORY, and IEEE TRANSACTIONS ON INFORMATION FORENSICS AND SECURITY.

Yasamin Mostofi (Fellow, IEEE) received the B.S. degree from the Sharif University of Technology, Tehran, Iran, and the M.S. and Ph.D. degrees from Stanford University, Stanford, CA, USA. She is currently a Professor with the Department of Electrical and Computer Engineering, University of California, Santa Barbara, Santa Barbara, CA, USA. Her research spans two broad areas of wireless systems and robotics/control. Current high-level research thrusts include RF sensing for several different applications such as through-wall imaging, occupancy analytics, context inference, smart health, and smart spaces; and communication-aware robotics, UAV-assisted connectivity, and joint robotic path planning and communication. She was the recipient of the Presidential Early Career Award for Scientists and Engineers, Antonio Ruberti Prize from the IEEE Control Systems Society, National Science Foundation CAREER Award, and the IEEE Outstanding Engineer Award of Region 6. Her research has been featured in prominent news outlets such as the BBC, New Scientist, Huffington Post, Daily Mail, Engadget, TechCrunch, NSF Science360, ACM News, and *IEEE Spectrum*. She was in many leadership capacities including serving on the inaugural editorial board of Nature Partner Journals (NPJ) on Wireless Technology, a Technical Program Co-Chair for ACM MobiCom 2022, serving on the Board of Governors for IEEE Control Systems Society, and a Senior Editor of IEEE TRANSACTIONS ON CONTROL OF NETWORK SYSTEMS.

Ashutosh Sabharwal (Fellow, IEEE) is currently the Ernest D. Butcher Professor of electrical and computer engineering with the Computer Science Department, Rice University, Houston, TX, USA. His ongoing work in wireless focuses on joint wireless communications & imaging and large-scale experimental platforms. He was a co-inventor of full-duplex wireless, which has been adopted in communications standards. He also led the WARP and RENEW projects, which were instrumental in establishing open-source wireless research platforms. He was awarded the 2017 IEEE Jack Neubauer Memorial Award, 2018 IEEE Advances in Communications Award, the 2019, 2021 & 2025 ACM Test-of-Time Awards, the 2019 ACM MobiCom Community Contribution Award, and the 2023 ICC Best Paper Award. He is a Fellow of ACM and the National Academy of Inventors.